Modelling of Coupled Cross-Flow/In-Line Vortex-Induced Vibrations Using Double Duffing and Van Der Pol Oscillators

Narakorn Srinil & Hossein Zanganeh

Department of Naval Architecture & Marine Engineering, University of Strathclyde,

Henry Dyer Building, Glasgow G4 0LZ, Scotland, UK, Contact email: narakorn.srinil@strath.ac.uk

Research Highlights

- An advanced model for predicting coupled cross-flow/in-line VIV of cylinders is presented
- The model has been calibrated and validated for cylinders with different mass/damping ratios
- The model captures important VIV characteristics such as hysteresis and figure of eight
- Numerical and experimental results are in good qualitative and quantitative agreement
- The effects of cylinder geometrical nonlinearities and natural frequency ratio are underlined

Modelling of Coupled Cross-Flow/In-Line Vortex-Induced Vibrations Using Double Duffing and Van Der Pol Oscillators

Narakorn Srinil* & Hossein Zanganeh

Department of Naval Architecture & Marine Engineering, University of Strathclyde,

Henry Dyer Building, Glasgow G4 0LZ, Scotland, UK

Abstract

Many studies have typically applied a linear structural spring-mass-damper oscillator and a van der Pol wake oscillator to model a one-dimensional cross-flow vortex-induced vibration (VIV). In this study, an advanced model for predicting a two-dimensional coupled cross-flow/in-line VIV of a flexibly-mounted circular cylinder in a uniform flow is proposed and validated. The ensuing dynamical system is based on double Duffing-van der Pol (structural-wake) oscillators with the two structural equations containing both cubic and quadratic nonlinear terms. The cubic nonlinearities capture the geometrical coupling of cross-flow/in-line displacements excited by hydrodynamic lift/drag forces whereas the quadratic nonlinearities allow the wake-cylinder interactions. Some empirical coefficients are calibrated against published experimental results to establish a new generic analytical function accounting for the dependence of VIV on a physical mass and/or damping parameter. By varying flow velocities in the numerical simulations, the derived low-order model captures several important VIV characteristics including a two-dimensional lock-in, hysteresis phenomenon and figure-of-eight trajectory tracing the periodically coupled in-line/cross-flow oscillations with their tuned two-to-one resonant frequencies. By making use of a newly-derived empirical formula, the predicted maximum cross-flow/in-line VIV amplitudes and associated lock-in ranges compare well with several experimental results for cylinders with low/high mass or damping ratios. Moreover, the parametric studies highlight the important effect of geometrical nonlinearities through new displacement coupling terms and the ratio of in-line to cross-flow natural frequencies of the freely-vibrating cylinder.

Keywords: Vortex-Induced Vibration (VIV), Circular Cylinder, Cross-Flow Oscillation, In-Line Oscillation, Fluid-Structure Interaction, Wake Oscillator

*Corresponding author: narakorn.srinil@strath.ac.uk; tel. +44 1415483463; fax +44 1415522879

Nomenclature

A_x/D, A_y/D	Dimensionless in-line and cross-flow amplitudes
A_{xm}/D, A_{ym}/D	Dimensionless maximum attainable amplitudes
a, b, c	Coefficients of best-fit analytical functions
C_D, C_L	Unsteady drag and lift coefficients
C_{D0}, C_{L0}	Drag and lift coefficients of a stationary cylinder
C_{fx}, C_{fy}	Hydrodynamic damping coefficients
C_M	Added mass coefficient
C_{sx}, C_{sy}	Structural viscous damping coefficients
D	Diameter of a circular cylinder
f^*	Ratio of cylinder in-line to cross-flow natural frequencies
F_D, F_L	Fluctuating drag and lift forces
F_x, F_y	Hydrodynamic forces in streamwise and transverse directions
K_x, K_y	Spring stiffness
M_D, M_L	System mass parameters
m_{fx}, m_{fy}	Fluid added masses
m_{sx}, m_{sy}	Cylinder masses
p, q	Reduced vortex drag and lift coefficients
S_G	Skop-Griffin parameter
St	Strouhal number
S_x, S_y	Excitation terms simulating the effect of cylinder on the near wake
t	Dimensionless time
T	Dimensional time
V	Uniform flow velocity
V_r	Reduced flow velocity
V_{rxm}, V_{rym}	Reduced velocities at maximum attainable amplitudes
X, Y	Dimensional in-line and cross-flow displacements
x, y	Dimensionless in-line and cross-flow displacements
α^*_x, α^*_y, β^*_x, β^*_y	Dimensional geometrically-nonlinear coefficients
α_x, α_y, β_x, β_y	Dimensionless geometrically-nonlinear coefficients
γ	Stall parameter
ε_x, ε_y	Wake coefficients
θ	Angle of attack of the flow relative to the cylinder
λ_x, λ_y	Combined fluid-structural damping terms
Λ_x, Λ_y	Wake-cylinder coupling coefficients
μ_x, μ_y, m^*_x, m^*_y, m^*	Mass ratios
ξ_x, ξ_y, ξ	Structural reduced damping coefficients
ρ	Fluid density
Ω	Ratio of vortex-shedding to cylinder cross-flow natural frequencies
ω_f	Vortex-shedding angular frequency
ω_{nx}, ω_{ny}	Structural natural frequencies in still water

1. Introduction

Vortex-induced vibration (VIV) is a fundamental phenomenon commonly encountered in various practical engineering applications and physical sciences where a fluid flow dynamically excites and interacts with a bluff solid/flexible structure. In connection with the oil & gas industry, the risk of VIV is one of the most technically and economically critical concerns in the analysis and design of key offshore cylindrical structures including risers, mooring cables, pipelines and subsea components. Although a basic mechanism of the VIV occurrence is well known (Blevins, 1990) and VIV-related subjects have been extensively investigated (Bearman, 2011; Sarpkaya, 2004; Williamson and Govardhan, 2004), a completely reliable simulation model for predicting the associated fluid-structure interaction and nonlinear dynamical behavior is still needed. Owing to the complexity of the vortex hydrodynamics, the intrinsic mechanism of the structure, the overall elasto-hydro nonlinearities, the influence of several mechanical/physical parameters, and the necessity to calibrate and validate the simulation model with substantial experimental data, modelling of VIV remains a challenging theme.

VIV occurrences are widely categorized as cross-flow or in-line VIV in which the structure oscillates in the direction transverse to or aligned with the flow, respectively. Many studies have focused on the modelling of pure cross-flow VIV excited by the lift force because of its usually observed largest response (Bishop and Hassan, 1964; Gabbai and Benaroya, 2005; Hartlen and Currie, 1970; Sarpkaya, 2004). Very little is known about the effect of oscillating drag force, the ensuing in-line VIV, the coupling of cross-flow/in-line VIV, the dependence on system parameters and how to realistically model these features. Several recent experimental studies have evidenced the significant effect of in-line VIV (Dahl et al., 2006; Dahl et al., 2010; Jauvtis and Williamson, 2004; Jeon and Gharib, 2001); due to a doubled oscillating frequency, this can contribute – as much as the cross-flow VIV – to the current-induced fatigue damage of structures (Vandiver and Jong, 1987). Computational flow visualizations have also illustrated different vortex mode patterns in the wake behind cylinders oscillating with one-degree-of-freedom (DOF) vs. two-DOF displacements (Karanth et al., 1995). Due to combined lift/drag forces associated with the shedding vortices and the fact that actual underwater structures possess multiple natural frequencies in different directions, a condition of coupled cross-flow/in-line VIV is certainly achievable in most practical situations which can be responsible for dangerously-amplified dynamics. Nevertheless, most of the numerical tools currently used in the engineering industry are limited to the analysis of cross-flow-only VIV (Chaplin et al., 2005; Srinil, 2010, 2011; Srinil et al., 2009). Therefore, an advanced predictive model accounting for the coupled

cross-flow/in-line, two-dimensional (2-D) or 2-DOF VIV, as proposed in the present study, would be worthwhile from a practical and industrial viewpoint.

Several researchers have applied phenomenological models to describe a fluctuation of the lift force with a van der Pol-based wake oscillator (Bishop and Hassan, 1964; Facchinetti et al., 2004; Farshidianfar and Zanganeh, 2010; Hartlen and Currie, 1970; Skop and Balasubramanian, 1997; Srinil, 2010; Stappenbelt, 2011). To simulate the VIV of circular cylinders in uniform flows, a set of coupled (linear) structural and (nonlinear) wake oscillators have typically been considered. Some general aspects – pertaining to the recent use of wake-structure oscillator models – should be summarized:

- A standard linear mass-spring-damper system is used to describe the cylinder oscillation. The effect of structurally geometrical nonlinearities has often been disregarded.
- The coupling of wake and cylinder motions is recognized through a linear term in the wake equation depending on the cylinder displacement, velocity or acceleration.
- Empirical coefficients in the wake oscillator rely upon calibration with experimental amplitude data; however, these coefficients are generally assumed to be constant.
- A complete wake-structure oscillator model for simulating the coupling of cylinder cross-flow/in-line motions excited by the hydrodynamic lift/drag forces is lacking.

To overcome some of the aforesaid issues, the objectives of the present study are to (i) advance the wake-structure oscillator models to realistically simulate the coupling of cross-flow/in-line VIV of flexibly-mounted circular cylinders in uniform flows, (ii) calibrate empirical coefficients by accounting for the important mass/damping parameters, and (iii) validate the predicted 2-DOF VIV responses with recently published experimental data in terms of maximum attainable amplitudes and lock-in ranges. Overall, the main contributions of this paper are the introduction of new cubic nonlinear terms in the two structurally coupled (Duffing-type) oscillators defining cylinder cross-flow/in-line motions, the inclusion of quadratic nonlinear terms entailing the wake-structure interaction through the consideration of relative velocities of the cylinder and the incoming flow, the use of a variable empirical wake coefficient through a newly derived function, and the effect of in-line-to-cross-flow natural frequency ratio of the cylinder. Some recent studies have shown the effect of geometrical nonlinearities on cross-flow VIV (Hover, 1998; Srinil, 2010; Stappenbelt, 2010) whereas the present work aims to highlight such potential effect on coupled cross-flow/in-line VIV.

The paper is structured as follows. In Section 2, a low-order predictive model for a circular cylinder undergoing 2-DOF VIV is proposed based on two sets of nonlinear structure-wake equations. In Section 3, new generic analytical functions of empirical wake coefficients are identified through the

best-fits of relevant experimental results. The analysis and prediction of coupled cross-flow/in-line VIV is systematically performed in Section 4 which highlights the effects of several important parameters and fundamental 2-D VIV behaviors, and displays good comparisons with experimental results in the literature. Also, the overall effect of new modelled terms and empirical coefficients on the predicted VIV response is summarized. The paper ends with the conclusions in Section 5.

2. Two-Dimensional VIV Model with Combined Structural/Hydrodynamic Nonlinearities

A low-order mathematical model simulating the nonlinear 2-D free vibration of an elastically-supported circular cylinder in a uniform steady flow with a velocity V is developed. The cylinder is assumed to be infinitely long such that a mechanical spring-mass-damper system (i.e. the structural oscillator) can be used to model the cylinder dynamic response. As displayed in Fig. 1, the cylinder of diameter D is constrained by a two-directional four-spring system, freely oscillating in both in-line (streamwise) X and cross-flow (transverse) Y directions with O at the cylinder centre being the origin of the co-ordinates. In contrast to several existing VIV models which typically consider a linear structural oscillator to describe the cylinder – mostly Y – displacement (Gabbai and Benaroya, 2005), the effect of geometric nonlinearities (i.e. spring nonlinear stiffness or restoring force) of the oscillating cylinder is herein accounted for alongside the hydrodynamic nonlinearities governing the fluctuation of the vortex-induced lift/drag forces.

By permitting the cylinder to oscillate in both cross-flow/in-line directions, experimental results (Moe and Wu, 1990; Sarpkaya, 1995; Stappenbelt, 2011) showed that the associated cylinder amplitudes noticeably increase in comparison with the pure cross-flow VIV, owing to the greater influence of fluid-structure interaction. Depending on system parameters, the cross-flow maximum amplitudes in the 2-D VIV case may achieve such high values as 1.5D (Dahl et al., 2006) or even 2D (Leong and Wei, 2008), being much greater than typical values of about 1D observed in the cross-flow-only VIV (Govardhan and Williamson, 2000; Khalak and Williamson, 1999). According to the large-amplitude response, the axial stretching of the springs may become intrinsically nonlinear, being amplitude-dependent and bi-directionally coupled. Recently, the applied VIV analysis of flexible curved/straight structures has highlighted how the multi-mode interactions in conjunction with structural nonlinearities play a crucial role in both numerical VIV prediction and comparison with experimental results (Srinil, 2010). Based on these findings, two nonlinearly-coupled structural oscillators in conjunction with two nonlinear wake oscillators are proposed for advanced 2-D VIV modelling and simulation.

The nonlinear equations of motion of the 2-D freely-oscillating cylinder are derived based on the actual physics of the moving springs, similar to the formulation described by Bush (1992) in a one-directional spring case. By considering four coupled springs as in Fig. 1, the geometrically-nonlinear oscillators governing the in-line and cross-flow vibrations of the cylinder may be expressed as

$$(m_{sx}+m_{fx})\ddot{X}+\left(C_{sx}+C_{fx}\right)\dot{X}+K_x\left(X+\alpha_x^*X^3+\beta_x^*XY^2\right)=F_x, \tag{1}$$

$$(m_{sy}+m_{fy})\ddot{Y}+\left(C_{sy}+C_{fy}\right)\dot{Y}+K_y\left(Y+\alpha_y^*Y^3+\beta_y^*YX^2\right)=F_y, \tag{2}$$

where a dot denotes differentiation with respect to the dimensional time T, X and Y are dimensional in-line and cross-flow displacements, m_s, m_f, C_s, C_f and K the associated cylinder mass, fluid added mass, viscous damping, hydrodynamic damping and spring stiffness coefficients, respectively, with co-subscripts x and y identifying properties in these directions. We assume $m_{fx} = m_{fy} = m_f$ and $C_{fx} = C_{fy} = C_f$, with $m_f = \pi\rho D^2 C_M/4$ and $C_f = (2\pi \mathrm{St} V/D)\gamma\rho D^2$ (Facchinetti et al., 2004). Herein ρ is the fluid density, C_M the added mass coefficient (assumed to be unity for a circular cylinder (Blevins, 1990)), St the so-called Strouhal number (Sarpkaya, 2004), and γ the stall parameter which is directly related to the sectional mean drag coefficient and assumed to be a constant equal to 0.8 (Facchinetti et al., 2004). The quantities α^*_x, α^*_y, β^*_x, and β^*_y are geometrical coefficients pertaining to the moving spring-mass system. Note that Eqs. (1) and (2) are so-called Duffing oscillators (Nayfeh, 1993) whose cubic-type nonlinear terms capture the axial stretching feature (X^3, Y^3) and physical coupling of cross-flow/in-line motions (XY^2, YX^2). The use of two coupled Duffing oscillators can also be found in some other scientific applications (Raj and Rajasekar, 1997).

For an oscillating cylinder, F_x and F_y are the time-varying hydrodynamic forces determined by resolving the sectional drag F_D and lift F_L forces – which are considered to be non-coincident with the horizontal and vertical axes (see Fig. 1) – into the streamwise and transverse directions. By accounting for the relative velocities of the incoming flow and the cylinder streamwise motion, assuming a small angle of attack θ of the flow relative to the cylinder (Blevins, 1990), and omitting the mean drag component, F_x and F_y may be expressed as (Wang et al., 2003)

$$F_x = F_D\cos\theta - F_L\sin\theta \approx F_D - F_L\,\dot{Y}/V\,, \tag{3}$$

$$F_y = F_L\cos\theta + F_D\sin\theta \approx F_L + F_D\,\dot{Y}/V\,. \tag{4}$$

Accordingly, the unsteady drag and lift force components are given by

$$F_D = \frac{1}{2}\rho D V^2 C_D, \qquad F_L = \frac{1}{2}\rho D V^2 C_L, \tag{5}$$

where C_D and C_L are the time-varying drag and lift coefficients, respectively. By introducing the reduced vortex lift coefficients as $p = 2C_D/C_{D0}$ and $q = 2C_L/C_{L0}$ (Facchinetti et al., 2004) in which C_{D0} and C_{L0} are the associated drag and lift coefficients of a stationary cylinder (assumed as C_{D0}=0.2 (Currie and Turnbull, 1987) and C_{L0}=0.3 (Blevins, 1990)), the time variation of the fluid vortex variables p and q may follow the self-excitation nature of the van der Pol-based wake oscillators described by

$$\ddot{p} + 2\varepsilon_x \omega_f \left(p^2 - 1\right)\dot{p} + 4\omega_f^2 p = S_x, \tag{6}$$

$$\ddot{q} + \varepsilon_y \omega_f \left(q^2 - 1\right)\dot{q} + \omega_f^2 q = S_y. \tag{7}$$

Herein, $\omega_f = 2\pi \mathrm{St} V/D$ is the vortex-shedding angular frequency, S_x and S_y are the excitation terms simulating the effect of cylinder motion on the near wake, ε_x and ε_y the wake empirical coefficients. The coupling and interaction between the fluid and the structure is captured through the excitation terms F_x (Eq. 1), F_y (Eq. 2), S_x (Eq. 6) and S_y (Eq. 7). Whilst F_x and F_y depend on the projection of oscillating drag/lift forces through Eqs. (3)-(5) accounting for the reduced vortex coefficients p and q, the influence of S_x and S_y may be assumed to be linearly proportional to the displacement (Noack et al., 1991), velocity (Skop and Balasubramanian, 1997) or acceleration (Facchinetti et al., 2004) of the cylinder. Based on 1-D VIV studies, Facchinetti et al. (2004) have examined the effect of the coupling term S_y on the VIV modelling and finally suggested the use of an acceleration model. Similarly, we assume in the 2-D VIV modelling that

$$S_x = \Lambda_x \ddot{X}/D, \quad S_y = \Lambda_y \ddot{Y}/D, \tag{8}$$

where Λ_x and Λ_y are the empirical coupling parameters adopted equally as Λ_x=Λ_y=12 based on the suggested Λ_y=12 in Facchinetti et al. (2004). This assumption would allow us to focus on the scaling and calibration of other control parameters (ε, α, β): see Sections 3, 4.1 and 4.2.

By introducing the dimensionless time $t = \omega_{ny}T$, displacements $x = X/D$ and $y = Y/D$, the nonlinearly-coupled Eqs. (1), (6), (2) and (7) with four unknown variables (x, p, y, q) – simulating coupled in-line (x) and cross-flow (y) VIV due to fluctuating drag (p) and lift (q) fluid forces – become

$$\ddot{x} + \lambda_x \dot{x} + f^{*2}\left(x + \alpha_x x^3 + \beta_x x y^2\right) = M_D \Omega^2 p - 2\pi M_L \Omega^2 \left(q\,\dot{y}/V_r\right), \tag{9}$$

$$\ddot{p} + 2\varepsilon_x \Omega \left(p^2 - 1\right)\dot{p} + 4\Omega^2 p = \Lambda_x \ddot{x}, \tag{10}$$

$$\ddot{y} + \lambda_y \dot{y} + y + \alpha_y y^3 + \beta_y y x^2 = M_L \Omega^2 q + 2\pi M_D \Omega^2 \left(p\,\dot{y}/V_r\right), \tag{11}$$

$$\ddot{q} + \varepsilon_y \Omega \left(q^2 - 1 \right) \dot{q} + \Omega^2 q = \Lambda_y \ddot{y}, \tag{12}$$

where Ω = StV_r is equivalent to ω_f/ω_{ny}, being the ratio of vortex-shedding frequency to the cylinder cross-flow natural frequency in still water, with $V_r = 2\pi V/\omega_{ny}D$ the so-called reduced flow velocity parameter (Sarpkaya, 2004). The ratio of structural natural frequencies in X and Y directions is given by $f^* = \omega_{nx}/\omega_{ny}$ where

$$\omega_{nx} = \sqrt{\frac{K_x}{m_{sx} + m_f}}, \quad \omega_{ny} = \sqrt{\frac{K_y}{m_{sy} + m_f}}. \tag{13}$$

M_D and M_L are the system mass parameters defined as

$$M_D = \frac{C_{D0}}{2} \frac{1}{8\pi^2 \mathrm{St}^2 \mu_x}, \quad M_L = \frac{C_{L0}}{2} \frac{1}{8\pi^2 \mathrm{St}^2 \mu_y}, \tag{14}$$

in which the mass ratios μ_x and μ_y are expressed as (Facchinetti et al., 2004)

$$\mu_x = \frac{m_{sx} + m_f}{\rho D^2}, \quad \mu_y = \frac{m_{sy} + m_f}{\rho D^2}. \tag{15}$$

The damping terms λ_x and λ_y, accounting for the effects of structural viscous damping and fluid added damping (stall term), are given by

$$\lambda_x = 2\xi_x f^* + \gamma\Omega / \mu_x, \quad \lambda_y = 2\xi_y + \gamma\Omega / \mu_y, \tag{16}$$

where ξ_x and ξ_y are the structural reduced damping coefficients. Note that the mass ratio definition in the literature is variable but it is widely recognized by the notation m^* (Williamson and Govardhan, 2004) relating to Eq. (15) by

$$m_x^* = 4\mu_x / \pi - C_M, \quad m_y^* = 4\mu_y / \pi - C_M. \tag{17}$$

In parametric studies, the mass ratio is herein referred to as m^*; the condition of $m^*_x = m^*_y = m^*$ is applied since practical offshore cylindrical structures generally have a circumferentially-uniform mass. However, some experimental studies have considered unequal m^*_x and m^*_y (Dahl et al., 2006; Moe and Wu, 1990) which would make calibration more complicated. With the same reason, $\xi_x = \xi_y = \xi$ is assumed. Finally, α_x, α_y, β_x, and β_y are the dimensionless counterparts of geometrical parameters α^*_x, α^*_y, β^*_x, and β^*_y, respectively, whose effects will be investigated in Section 4.1.

It is worth emphasizing that Eqs. (9) and (11) contain cubic (x^3, xy^2, y^3, x^2y) and quadratic ($q\dot{y}$, $p\dot{y}$) nonlinearities, the former capturing the axial stretching/structural coupling of x-y displacements and the

latter allowing the wake-cylinder interactions so do the linear terms in the right hand side of Eqs. (10) and (12). Some of these nonlinear terms may entail drift components (Nayfeh, 1993) but the latter are disregarded as attention is placed on the oscillating components. The cylinder natural frequency ratio f^* is a key physical parameter in addition to m^* and ξ which are embedded in M_D, M_L, λ_x and λ_y (Eqs. 13-17). The non-linearly coupled Eqs. (9)-(12) are numerically solved using a fourth-order Runge-Kutta scheme with an adaptive time step enabling the solution convergence and stability, and with assigned initial conditions at $t = 0$ of $x = y = 0$, $p = q = 2$ and zero velocities. The case of increasing V_r is generally considered. However, if a sudden jump of response amplitude occurs, V_r may also be decreasingly varied to capture a possible hysteresis. In all simulation cases, V_r is varied in steps of 0.1.

3. Identification of Empirical Coefficients Depending on System Mass and/or Damping

The analysis and prediction of coupled cross-flow/in-line VIV of circular cylinders based on Eqs. (9)-(12) depend on several empirical coefficients (ε_x, ε_y, Λ_x, Λ_y) and geometrically-nonlinear parameters (α_x, α_y, β_x, β_y). Fixed values of ε_y and Λ_y have recently been proposed for a 1-D VIV (Facchinetti et al., 2004) whereas a new set of ε_x, ε_y, Λ_x, Λ_y, α_x, α_y, β_x and β_y is herein proposed for a 2-D VIV. For a given m^*, ξ and f^*, these coefficients and parameters can be identified by calibrating the numerically-obtained in-line and cross-flow amplitudes (A_x/D and A_y/D) with experimental results and by accounting for some qualitative VIV behaviors. Owing to a large set of variables, it is impractical in a parametric study to capture the system dependence on all of these variables. Accordingly, $\varepsilon_x = 0.3$, $\Lambda_x = \Lambda_y = 12$ (Facchinetti et al., 2004), and $\alpha_x = \alpha_y = \beta_x = \beta_y = 0.7$ are preliminarily fixed whereas the ε_y-function is determined through the best fits of 2-D VIV experiment results in the case of varying (i) ξ (Blevins and Coughran, 2009), (ii) m^* (Stappenbelt et al., 2007) and (iii) $m^*\xi$ (Blevins and Coughran, 2009; Stappenbelt et al., 2007). After identifying the ε_y-functions, the sensitivity analysis of other coefficients/parameters will be carried out as in Sections 4.1 and 4.2. For a specific $f^* = 1$, Table 1 summarizes the test matrix from the two experiments by reporting the assigned ξ (Table 1a) or m^* (Table 1b), and the associated $m^*\xi$, along with the tuned ε_y deduced from relevant numerical-experimental calibrations. In the following, only A_y/D are plotted whereas combined A_x/D and A_y/D will be presented in Section 4.

By first considering the case of varying ξ with a fixed low mass $m^*= 5.4$ (Blevins and Coughran, 2009), Fig. 2 illustrates a comparison of numerically-predicted (lines) and experimentally-obtained (squares) A_y/D for $\xi = 0.002$ (Fig. 2a), 0.02, 0.05, 0.1, 0.2 and 0.4 (Fig. 2b). With the lowest $\xi = 0.002$, results with increasing (→) and decreasing (←) V_r are plotted in Fig. 2a which reveals the jump-up and

-down responses (denoted by dashed lines) and hysteresis of amplitudes around V_r = 8. The experimental and numerical maximum $A_y/D \approx 1.5$ and the associated lock-in ranges ($4 < V_r < 8$ or 10) are qualitatively and quantitatively comparable, although the numerical model underestimates the lower-amplitude branch ($V_r > 8$). Similar large maximum A_y/D values (1.5 and above) have also been reported by some other experiments, e.g. in Dahl et al. (2006). When ξ is increased by one (ξ=0.02, 0.05) or two (ξ=0.1, 0.2, 0.4) orders of magnitude, both numerical and experimental results in Fig. 2b show decreasing A_y/D as expected, being as small as $A_y/D \approx 0.1$ for $\xi = 0.4$. The numerical model also predicts the disappearing jump for high ξ = 0.05, 0.1, 0.2, 0.4. Table 1a shows, except ξ = 0.002 and 0.4, the increment of ε_y with increasing ξ. From a dynamical viewpoint, the decreasing A_y/D is feasible as ε_y mainly governs the nonlinear damping term (Eq. 12) regulating the self-excited and -limiting character of the VIV response (Gabbai and Benaroya, 2005); thus, as ε_y increases, the damping effect increases too while keeping other variables unchanged.

For a given low ξ=0.006 (Stappenbelt et al., 2007), Fig. 3 compares numerical (lines) and experimental (squares) A_y/D for various m^* = 2.36 (Fig. 3a), 3.68, 5.19, 6.54, 7.91, 8.76, 10.63 and 12.96 (Fig. 3b). It is seen that the predicted jump-up and -down responses occur almost the same V_r in Fig. 3a; nevertheless, the jump disappears in Fig. 3b for higher m^* = 7.91, 8.76, 10.63 and 12.96, similar to higher ξ cases in Fig. 2b. The maximum A_y/D as well as the associated lock-in ranges decrease as m^* increases, in qualitative agreement with general experimental results (Jauvtis and Williamson, 2004). The model predicts a slight shift in V_r at the jump for high m^* values (Fig. 3b) but this is considered of secondary importance as far as the primary attention is placed on calibrating maximum amplitudes. Comparing the case with m^* = 5.4 and ξ = 0.002 in Fig. 2a to the case with m^* = 5.19 and ξ = 0.006 in Fig. 3b, the former shows a greater maximum A_y/D due to a lower ξ. Although both cases have comparable m^*, such comparison emphasizes the role of damping in the VIV as suggested by Klamo et al. (2006). Similar to the increasing ξ case in Table 1a, Table 1b shows the increment of tuned ε_y with increasing m^*; i.e. both cases yield the decreasing A_y/D (Figs. 2 and 3).

By plotting and applying variable curve fitting to the relationship of ξ and ε_y in Table 1a, a cubic polynomial-based function is chosen as the best-fit $\varepsilon_y(\xi)$ function given by

$$\varepsilon_y = a_3\xi^3 + a_2\xi^2 + a_1\xi + a_0, \tag{18}$$

where a_0, a_1, a_2, and a_3 are polynomial coefficients approximately equal to 0.0048, 0.0274, 0.8266 and -2, respectively. In the same way, curve fitting to the relationship of m^* and ε_y in Table 1b entails the best-fit exponential $\varepsilon_y(m^*)$ function as

$$\varepsilon_y = b_1 e^{\left[b_2 m^*\right]}, \tag{19}$$

where b_1=0.0045 and b_2=0.228. In the third scenario, both m^* and ξ are simply combined as $m^*\xi$ and the relationship of $m^*\xi$ and ε_y taking into account the information from both Tables 1a and 1b can be described by the best-fit Gaussian $\varepsilon_y(m^*\xi)$ function expressed as

$$\varepsilon_y = c_1 e^{-\left[\frac{m^*\xi - c_2}{c_3}\right]^2} + c_4 e^{-\left[\frac{m^*\xi - c_5}{c_6}\right]^2}, \tag{20}$$

where c_1=0.0366, c_2=0.0762, c_3=0.02046, c_4=0.02995, c_5=1.464 and c_6=1.103. The above nonlinear functions enable us to capture the dependence of VIV on m^* (Eq. 18), ξ (Eq. 19) or $m^*\xi$ (Eq. 20) through the wake empirical coefficient ε_y.

To validate the above functions and identify which of them will be used in the subsequent studies, we next apply Eqs. (18)-(20) along with Eqs. (9)-(12) to simulate 2-D VIV responses of a recent experimental model of Jauvtis and Williamson (2004) which considered f^* = 1 with two measurement sets: (i) m^* = 2.6 and ξ = 0.0025, (ii) m^* = 7 and ξ = 0.0007. Experimental A_y/D (squares) are plotted against numerical A_y/D (lines) in Figs. 4a (case i) and 4b (case ii). The corresponding values of $\varepsilon_y(\xi)$, $\varepsilon_y(m^*)$ and $\varepsilon_y(m^*\xi)$ are 0.0048, 0.0042 and 0.0052 in Fig. 4a, whereas they are 0.0048, 0.0116 and 0.0052 in Fig. 4b, respectively. Note that these ε_y values are much smaller than the value 0.3 proposed by Facchinetti et al. (2004). Overall, a good agreement between experimental results and numerical predictions based on three different functions is found in the higher mass-damping ($m^*\xi$ = 0.0064) case (Fig. 4a), showing both the response jumps and overall amplitude (initial, upper and lower) branches (Jauvtis and Williamson, 2004). However, in the lower mass-damping ($m^*\xi$ = 0.0048) case (Fig. 4b), discrepancies in maximum A_y/D between experimental and numerical results are remarkable when the latter are based on $\varepsilon_y(\xi)$ and $\varepsilon_y(m^*\xi)$ functions owing to their fixed and comparable ε_y being 0.0048 and 0.0052, respectively. Based on these observations, the $\varepsilon_y(m^*)$ function based on Eq. (19) is preferably used in the following parametric investigations.

4. Analysis and Prediction of Coupled Cross-Flow/In-Line VIV

Coupled cross-flow/in-line VIV responses of circular cylinders with different m^*, ξ and f^* are now parametrically investigated to highlight the effect of key parameters and several VIV features. By way of examples, experimental input data (Blevins and Coughran, 2009; Dahl et al., 2006; Jauvtis and Williamson, 2004; Stappenbelt et al., 2007) whose Reynolds numbers are within the sub-critical flow regime are considered. A reference set of coefficients and parameters in the computation is based on ε_x

= 0.3, $\Lambda_x = \Lambda_y = 12$, $\alpha_x = \alpha_y = \beta_x = \beta_y = 0.7$, and the $\varepsilon_y(m^*)$ function deduced from the calibration in Section 3.

4.1 Influence of Cylinder Geometrical Nonlinearities and Natural Frequency Ratio

The influence of cylinder geometrical nonlinearities is first discussed based on the experimental data of Stappenbelt et al. (2007) with $m^* = 2.36$ and $\xi = 0.006$ (Fig. 3a). Numerical A_x/D and A_y/D results are plotted in Figs. 5 and 6 for f^*=1 and 2, respectively. Four simulation cases are performed with (i) neglected in-line nonlinearities α_x=β_x=0 (red lines), (ii) neglected cross-flow nonlinearities α_y=β_y=0 (green lines), and (iii) neglected in-line/cross-flow nonlinearities α_x=β_x=α_y=β_y= 0 (pink lines), in comparison with the full coupling benchmark case (iv) with α_x=β_x=α_y=β_y=0.7 (blue lines) and experimental results (squares). Note that experimental results are unavailable in the f^*=2 case.

Overall, simulation results reveal how omitting cross-flow and/or in-line nonlinearities can significantly affect the prediction of A_x/D and A_y/D, depending also on the specified f^*. With f^*=1 and $\alpha_x = \beta_x = 0$ (red vs. blue lines), the in-line nonlinearities have a greater effect on A_x/D (Fig. 5a) than A_y/D (Fig. 5b). Nevertheless, the bent-to-right responses still qualitatively exhibit the hardening-spring and jump (dashed lines) behaviors as in the full-coupling and experimental cases. When $\alpha_y = \beta_y = 0$ (green vs. blue lines), it is worth remarking on some quantitative as well as qualitative changes. Both A_x/D and A_y/D responses increase and appear nearly vertical with a vanishing jump, similar to a typical linear resonant damped response. As a result, the maximum amplitudes (especially A_x/D) shift towards V_r = 5 lower than V_r = 9 in the benchmark case. This shift of response maxima is in qualitative agreement with experimental results of Stappenbelt (2011) with varying cubic nonlinearities. By further imposing α_x=β_x=α_y=β_y=0 and comparing with the previous α_y=β_y=0 case (pink vs. green lines), A_y/D appear unchanged whereas A_x/D noticeably drop. These highlight how the cross-flow (in-line) geometric nonlinearities have a significant impact on both x and y (mostly x) responses. Overall, the $\alpha_x = \alpha_y = \beta_x = \beta_y = 0.7$ case provides the best fit to experimental results (squares).

With f^*=2, both in-line/cross-flow geometrical nonlinearities now play a significant role in both A_x/D (Fig. 6a) and A_y/D (Fig. 6b) diagrams which display distinctive dynamic scenarios amongst all the compared four cases, quantitatively and qualitatively. The maximum A_y/D occurs with the $\alpha_y = \beta_y = 0$ case whereas the maximum A_x/D occurs with the $\alpha_x = \beta_x = \alpha_y = \beta_y = 0$ case. The combined α_y- and β_y-based terms are found to be solely responsible for a jump as in Fig. 5 (see blue vs. red lines). With respect to the benchmark case, A_x/D (A_y/D) amplitudes increase (slightly decrease) when varying the cylinder frequency ratio from f^*=1 (Fig. 5) to f^* = 2 (Fig. 6), with A_x/D diagram in the f^*=1 case

displaying an emergence of a small first resonant peak around V_r = 2.5 (Fig. 5a). This is possibly due to a primary resonance between the wake and cylinder in-line frequencies. Overall, increasing f^* enhances the coupling and interaction of A_x/D and A_y/D through system cubic/quadratic nonlinearities.

4.2 Influence of Wake-Cylinder Coupling and In-Line Wake Coefficient

The influence of the acceleration coupling terms (Λ_x, Λ_y) and the in-line wake coefficient (ε_x) (Eqs. 10 and 12) on the prediction of 2-D VIV is next discussed based on the experimental data of Stappenbelt et al. (2007) with m^* = 2.36, ξ = 0.006 and f^*=1. By individually varying (i) Λ_y, (ii) Λ_x and (iii) ε_x, a comparison of A_x/D and A_y/D with respect to the benchmark case (Λ_y = Λ_x = 12 and ε_x = 0.3) is displayed in Figs. 7a and 7b (i), Figs. 7c and 7d (ii), and Figs. 7e and 7f (iii), respectively.

As Λ_y increases, it can be seen in Figs. 7a and 7b that overall amplitudes become greater, widening the associated lock-in ranges. This highlights a role played by the cross-flow acceleration coupling term in Eq. (12). On the contrary, the variation of Λ_x has a negligible effect on 2-D amplitudes as shown in Figs. 7c and 7d. This may be attributed to the small A_x/D and, correspondingly, the negligible contribution of cylinder in-line accelerations through Eq. (10).

With regard to varying ε_x, a noticeable feature should be mentioned via Fig. 7e. In particular, the numerical model predicts two resonant peaks in the in-line amplitude diagram (Fig. 7e) as in Figs. 5a, 7a and 7c, with the first resonant peak occurring at a low reduced velocity range ($2 < V_r < 4$) and increasing with decreasing ε_x. The first and second peaks in Fig. 7e are reminiscent of the second and third lock-in ranges of in-line oscillations, respectively, with the asymmetric vortex shedding in the cylinder wake (Currie and Turnbull, 1987; Jauvtis and Williamson, 2004). Based on some other trial simulations (not shown herein), it has been found that the first such peak would disappear if the in-line wake frequency in Eq. (10) was set equal to the cross-flow wake frequency in Eq. (12). As for the main 2-D lock-in range ($4 < V_r < 10$) (Jauvtis and Williamson, 2004), numerical results in Figs. 7e and 7f show a small ε_x effect on A_x/D and A_y/D. By comparing overall numerical and experimental results in Figs. 5-7, the reference set of coefficients $\Lambda_x = \Lambda_y = 12$, $\varepsilon_x = 0.3$ and parameters $\alpha_x=\beta_x=\alpha_y=\beta_y=0.7$ is the preferred option to be assumed in subsequent studies.

4.3 Influence of Mass/Damping Ratios and The Griffin Plots

The proposed wake-structure oscillator model is now used to predict and investigate the effect of m^* and ξ on the in-line response. In accordance with cross-flow responses shown in Figs. 2a and 2b (with varying ξ), Figs. 3a and 3b (with varying m^*), Figs. 4a and 4b (with varying $m^*\xi$), the predicted in-line responses in the f^*= 1 case are now displayed against experimental results of Blevins and Coughran

(2009), Stappenbelt et al. (2007), Jauvtis and Williamson (2004) in Figs. 8a (ξ= 0.002, 0.02), 8b (m^* = 2.36, 3.68) and 8c ($m^*\xi \approx$ 0.0064, 0.0048), respectively.

Overall, there is good agreement between numerical and experimental results which display two coexisting resonant peaks and maximum A_x/D values about 0.2-0.3 being much smaller than the maximum A_y/D in the range of 1.2-1.5. However, for the system with low ξ= 0.002, the numerical model in Fig. 8a further reveals a third intermediate peak with the highest amplitude (V_r = 6) (see also the corresponding orbital motion in Fig. 13b). The in-line amplitudes as well as associated lock-in ranges are seen to decrease with increasing ξ (Fig. 8a), m^* (Fig. 8b) and $m^*\xi$ (Fig. 8c), in the same way as the cross-flow amplitudes (Figs. 2-4).

Next, the influence of mass-damping on the 2-DOF VIV is demonstrated via the so-called Griffin plots. Over the last three decades, researchers had a discussion on whether the combined mass-damping, viz. the Skop–Griffin parameter $S_G=2\pi^3 St^2 m^*\xi$ (Williamson and Govardhan, 2004), could reasonably collapse different peak (typically cross-flow) amplitude data of different cylinders in the Griffin plots (Govardhan and Williamson, 2006). For the 2-D VIV study, observations in Blevins and Coughran (2009), Jauvtis and Williamson (2004) and Section 3 reveal the response dependence on both m^* and ξ. To further justify this, experimental data of Blevins and Coughran (2009), Stappenbelt et al. (2007) and Dahl et al. (2006) are considered; the associated maximum attainable (A_{ym}/D) and in-line (A_{xm}/D) amplitudes numerically (solid lines) and experimentally (symbols) obtained are compared in Figs. 9a and 9b, respectively. In addition, the associated reduced velocities at which A_{ym}/D and A_{xm}/D occur (V_{rym}, V_{rxm}) are also drawn vs. S_G in Figs. 9c and 9d. For each given m^* = 2.5 and 7, S_G is varied by altering ξ, and both f^* =1 and 2 are considered. Note that experimental results of Dahl et al. (2006) were based on $m_x^* \neq m_y^*$ (in the range of 3.3-5.7) and $\xi_x \neq \xi_y$ (in the range of 1.1-6.2 %), with f^* ranging from 1 to 1.90, those of Blevins and Coughran (2009) were based on m^* = 5.4 (varying ξ) and f^* = 1, and those of Stappenbelt et al. (2007) were based on ξ = 0.006 (varying m^*) and f^* = 1.

It can be seen in Figs 9a and 9b that, for a specific S_G, numerical results based on different fixed m^* and corresponding ξ are different. Both A_{ym}/D and A_{xm}/D decrease with increasing S_G, with the f^* = 2 (f^* = 1) case entailing greater in-line (cross-flow) responses for both assigned m^*. The difference in A_{xm}/D results between the f^* = 1 and 2 cases is pronounced particularly for the lower m^*=2.5: these emphasize a combined role played by both f^* and m^* captured by the proposed model. The predicted A_{xm}/D may reach a large value of 0.7 for a low S_G with f^* = 2. Apart from A_{ym}/D and A_{xm}/D, f^* also does affect their corresponding V_{rym} and V_{rxm} as shown in Figs. 9c and 9d, respectively. While V_{rym} of A_{ym}/D and V_{rxm} of A_{xm}/D in the case of m^* = 2.5 and f^* = 1 are comparable, those in other cases appear

significantly different. Increasing f^* tends to reduce V_{rym} for both m^*. However, V_{rxm} increases (decreases) as f^* increases for m^* = 7 (2.5) due to the greater first-peak (second-peak) A_{xm}/D, see, e.g., in the case of m^* = 7 vs. 2.6 (Fig. 8c). As for the experimental comparison, the associated A_{ym}/D and A_{xm}/D, as well as V_{rym} and V_{rxm}, also decrease with increasing S_G either due to the increasing ξ (Blevins and Coughran, 2009) or m^* (Stappenbelt et al., 2007), except some cases in Figs. 9b, 9c and 9d where $m_x^* \neq m_y^*$ and $\xi_x \neq \xi_y$ (Dahl et al., 2006).

By paying attention to the effect of m^*, a different scenario to show the capability of the proposed model in the 2-D VIV prediction is illustrated in Fig. 10 (f^*=1) based on two experimental datasets of Jauvtis and Williamson (2004) with fixed S_G = 0.0064 and Stappenbelt et al. (2007) with variable S_G. Former experimental results indicated that, at m^* higher than 6, the variation of m^* does not affect the peak amplitudes in either direction. Our numerical results agree with this but only for the in-line response shown in Fig. 10b. For the cross-flow response shown in Fig. 10a, numerical and experimental (Jauvtis and Williamson, 2004) results are in good agreement within the range $2 < m^* < 6$ showing decreasing A_{ym}/D with increasing m^*; for $m^* > 6$, however, the former continues to predict decreasing A_{ym}/D, instead of the nearly-constant A_{ym}/D from experiment. Although such a difference occurs at high m^*, both numerical A_{ym}/D and experimental results of Stappenbelt et al. (2007) are in good quantitative agreement throughout the considered m^* range. As for A_{xm}/D, Fig. 10b shows a good correspondence of overall numerical-experimental comparisons.

To further appreciate the combined effect of m^* and f^* on the 2-DOF VIV, Fig. 11 portrays the 3-D plots of amplitudes (A_y/D and A_x/D) vs. varying V_r and m^* for a given f^* = 1 (Figs. 11a and 11c) and f^* = 2 (Figs. 11b and 11d), respectively. The fixed ξ = 0.001 is considered as an example. It can be summarized that, by decreasing m^*, overall A_y/D and A_x/D and associated lock-in ranges increase whereby A_{ym}/D and A_{xm}/D occur at higher V_r. With f^* = 2, very large A_x/D amplitudes of nearly 1.2 are found in a low m^* range. This is a precarious circumstance since typical marine cylindrical structures have a low mass/damping and their natural frequencies could be tuned such that f^* = 2 (Srinil, 2010). In essence, for a very low $m^* \approx 0.5$, the model with f^* = 1 predicts the unbounded lock-in domain whose A_y/D and A_x/D persist throughout the considered V_r range (Figs. 11a and 11c). This occurrence of "resonance forever" (Govardhan and Williamson, 2002) is in good qualitative agreement with recent experimental results (Jauvtis and Williamson, 2004). Nevertheless, in the f^*=2 case, A_y/D and A_x/D tend to decline at higher V_r as shown in Figs. 11b and 11d.

4.4 Two-Dimensional Trajectories and Figures of Eight

It is of theoretical and practical importance to construct a 2-D (x-y) trajectory describing the relationship of cylinder in-line/cross-flow oscillations based on the proposed numerical model. In so doing, VIV simulations within the last ten cycles yielding steady A_{ym}/D and A_{xm}/D are considered for specific V_r in the neighborhood of hysteresis. Corresponding to Figs. 3a and 8b based on data of Stappenbelt et al. (2007) with $m^* = 2.36$, $\xi = 0.006$ and $f^* = 1$, the 2-D orbital motions in the cases of increasing (blue lines) and decreasing (red lines) flow velocities are drawn in Figs. 12a, 12b and 12c for V_r = 8, 9.25 and 9.45, respectively. Overall, the trajectories exhibit so-called figures of eight highlighting a tuned 2:1 resonance condition of in-line/cross-flow oscillating frequencies although inputting $f^* = 1$. For a specific V_r, depending on initial conditions, identical (Fig. 12a) or different (Figs. 12b and 12c) figures of eight may coexist with increasing and decreasing V_r cases.

It is now worth exploring which numerical terms play an influential role in the figure-eight appearance. Two cases are considered for $V_r = 9.45$ in comparison with the increasing flow case in Fig. 12c: firstly, the lift and drag wake frequencies in Eqs. (10) and (12) are assumed to be equal depending on the Strouhal frequency; secondly, the relative velocities between the flow and the cylinder are discarded thereby neglecting the quadratic nonlinear terms in the right-hand side of Eqs. (9) and (11). The associated simulation results are plotted with solid and dotted lines in Fig. 12d, respectively. It can be seen that both quantitative and qualitative discrepancies occur when neglecting the quadratic nonlinearities: the in-line (cross-flow) amplitudes considerably diminish (slightly increase) without showing the figure of eight. On the other hand, a similar figure of eight remains even though the wake in-line frequency has been altered. Other simulation V_r cases also agree with these observations. This highlights that as the 2:1 resonance and thus the figure of eight is generally associated with quadratic nonlinearities, neglecting the latter ($q\dot{y}$, $p\dot{y}$) – which capture the wake-cylinder interactions – may lead to the uncoupled in-line/cross-flow VIV response.

The influence of f^* on x-y trajectories is illustrated in Fig. 13 based on the experimental data of Blevins and Coughran (2009) with $m^* = 5.4$ and $\xi = 0.002$ (Figs. 2a and 8a). Simulation results with V_r = 4.5, 6, 7 and 7.6 are visualized in Fig. 13a, 13b, 13c and 13d, respectively, with six successive f^* = 1, 1.2, 1.4, 1.6, 1.8 and 2. It can be seen that, regardless of f^*, most of the x-y trajectories entail figure-eight orbits. They distinguish themselves depending on the corresponding in-line/cross-flow amplitudes, initial conditions, relative phases and the nearness or tuning of 2:1 resonant oscillating frequencies. These dual resonances confirm some recent experimental 2-D VIV results (Dahl et al., 2006; Dahl et al., 2010). Non-figure-eight trajectories are also found in some cases, for instance, in Fig.

13b with V_r = 6 and f^* = 1 or Fig. 13d with V_r = 7.6 and f^* = 1.2. Recently, elliptic *x-y* trajectories have been found and explained to be subject to a strong structural coupling (Kheirkhah et al., 2012).

4.5 Final Remarks

Based on the calibration with experimental results and substantial parametric studies, it can be concluded – from a modelling and prediction viewpoint – that important physical parameters m^*, ξ and f^* independently govern the 2-D VIV response. In general, strong coupling and interaction of cross-flow/in-line VIV motions take place in the fluid-structure system with low m^*, low ξ and f^* = 2, leading to large-amplitude responses whose A_{ym}/D (A_{xm}/D) may reach a high value of about 2 (1).

Depending on m^*, ξ and f^*, Table 2 summarizes the potential effect of geometrical nonlinearities through the newly proposed terms in the cylinder equations 9 and 11 (Figs. 5 and 6). The in-line cubic nonlinearities seem to have a quantitative effect on the overall motion by playing a greater role in the in-line response than the cross-flow response. Apart from the quantitative effect, the cross-flow cubic nonlinearities can also lead to a qualitatively different result if they are omitted whereby the jump and hysteresis disappear. These features are VIV amplitude-dependent: the higher the amplitudes the greater the geometrical nonlinear effects. As for the quadratic nonlinearities, it is essential to consider the relative velocities of the cylinder and the incoming flow in order to capture the 2:1 resonance and associated figure of eight (Figs. 12 and 13). The considered in-line wake frequency being twice the cross-flow wake frequency does not imply the figure of eight appearance but allows the occurrence of primary resonance (first peak) in the in-line response in addition to the main lock-in region involving cross-flow/in-line responses (Figs. 7 and 8).

As far as empirical coefficients are concerned, Table 3 summarizes the potential effect of ε_x, ε_y, Λ_x and Λ_y appearing in the wake equations (10 and 12). It can be seen that both ε_y and Λ_y have a high impact on cross-flow/in-line VIV predictions, possibly owing to the associated stronger wake strength and higher amplitude in the cross-flow direction (Figs. 2-4, 7a and 7b). In contrast, both main cross-flow/in-line responses are marginally influenced by a variation of ε_x and Λ_x (Figs. 7c-7f). Nevertheless, the tuning of ε_x could have a high impact on in-line VIV with respect to its first-peak resonance (Fig. 7e). Empirical functions for ε_y have been established (Eqs. 18-20) depending on m^* and/or ξ, and it is herein recommended to vary ε_y in the numerical prediction and perform a sensitivity analysis when using the proposed nonlinear wake-structure oscillators. Of course, new experimental tests, calibrations and validations are needed in order to improve Eqs. (18)-(20) and capture the influence of other

important parameters such as f^* and Reynolds number, in terms of both quantitative and qualitative aspects of coupled cross-flow/in-line VIV.

5. Conclusions

An advanced model for predicting a 2-D coupled cross-flow/in-line VIV of a flexibly-mounted circular cylinder in a uniform steady flow has been developed, calibrated and validated. The ensuing dynamical system is based on double Duffing-van der Pol (structural-wake) oscillators with the two structural equations containing cubic/quadratic nonlinear terms. The cubic nonlinearities describe the geometrical coupling of cross-flow/in-line displacements excited by hydrodynamic lift/drag forces whereas the quadratic nonlinearities allow the wake-cylinder interactions resulting from the relative velocities of the incoming flow and the oscillating cylinder. Some wake empirical coefficients have been identified based on calibration with experimental results in the literature, and new analytical functions accounting for the dependence of VIV on a physical mass and/or damping parameter have been established. These relationships would be useful for a future numerical implementation and experimental VIV analysis.

By varying flow velocities in the numerical simulations, the derived low-order model captures several fundamental VIV characteristics including 2-D lock-in, hysteresis phenomena and figure-of-eight trajectories tracing the periodically coupled in-line/cross-flow oscillations with their tuned two-to-one resonant frequencies. These figures of eight appear regardless of the specified ratio of cylinder in-line to cross-flow natural frequencies. By making use of a newly-derived empirical formula, the predicted cross-flow/in-line VIV amplitudes and associated lock-in ranges compare well with several experiment results for cylinders with low/high mass or damping ratios, by also revealing the occurrence of critical mass whereby maximum amplitudes exhibit the unbounded lock-in scenario. Prediction results also agree with recent experimental observations about how the Griffin plots – with the Skop-Griffin mass-damping parameter – may be insufficient to collapse maximum amplitude data of cylinders with different mass and damping.

Overall, the parametric investigations highlight the important effect of structural geometrical nonlinearities through new displacement coupling terms and the in-line-to-cross-flow natural frequency ratio of the freely-oscillating cylinder. By simulating the two-DOF VIV using the traditional linear (uncoupled) vs. newly-proposed nonlinear (coupled) structural models, the obtained dynamic responses appear quantitatively and/or qualitatively distinctive. The more-complete nonlinear model gives rise to a better agreement with relevant experimental results. Depending on the mass and damping, the nonlinear model predicts that the cylinder natural frequency ratio of two enhances the 2-D nonlinear

coupling, interaction and resonance by noticeably amplifying the in-line amplitudes and enlarging the associated lock-in ranges. From a practical viewpoint, combined cross-flow/in-line large-amplitude responses would be responsible for the significant fatigue damage in actual flexible cylinders such as marine risers, mooring cables and subsea pipelines.

Apart from enabling the 2-D VIV analysis and prediction by also confirming several meaningful VIV aspects observed experimentally, the proposed simulation model could be further improved by calibrating empirical coefficients with new experimental tests and/or computational fluid dynamics studies. In any case, the cylinder natural frequency ratio and geometrically nonlinear stiffness should be taken into account as one of the control parameters. Further analytical solution based on the proposed mathematical model could shed some light on the contributions of cubic/quadratic nonlinear terms and how they actually influence the vortex-induced dynamics and behaviors including the hysteresis, the multi-peak in-line response, the oscillating frequencies, the figure-of-eight character and relative phases. The hydrodynamic properties including added mass, added damping, oscillating lift and drag coefficients could also be systematically extracted. Finally, it is hoped that a combined analytical-numerical-experimental framework would pave the way for a forthcoming improvement of numerical predictive tools to be utilized by the offshore industry where VIV continues to render a detrimental concern towards deep-water engineering applications.

Acknowledgements

The authors are grateful to the scholarships provided by the University of Strathclyde and the Scottish Funding Council through the Scottish Overseas Research Students Awards Scheme (SORSAS).

References

Bearman, P.W., 2011. Circular cylinder wakes and vortex-induced vibrations. Journal of Fluids and Structures 27 (5–6), 648-658.

Bishop, R.E.D., Hassan, A.Y., 1964. The lift and drag forces on a circular cylinder oscillating in a flowing fluid, Proceedings of the Royal Society of London, pp. 51-75.

Blevins, R.D., 1990. Flow-Induced Vibrations. Van Nostrand Reinhold, New York.

Blevins, R.D., Coughran, C.S., 2009. Experimental investigation of vortex-induced vibration in one and two dimensions with variable mass, damping, and Reynolds number. Journal of Fluids Engineering 131 (10), 101202-101207.

Bush, A.W., 1992. Perturbation Methods for Engineers and Scientists CRC Press.

Chaplin, J.R., Bearman, P.W., Cheng, Y., Fontaine, E., Graham, J.M.R., Herfjord, K., Huera Huarte, F.J., Isherwood, M., Lambrakos, K., Larsen, C.M., Meneghini, J.R., Moe, G., Pattenden, R.J., Triantafyllou, M.S.,

Willden, R.H.J., 2005. Blind predictions of laboratory measurements of vortex-induced vibrations of a tension riser. Journal of Fluids and Structures 21 (1), 25-40.

Currie, I.G., Turnbull, D.H., 1987. Streamwise oscillations of cylinders near the critical Reynolds number. Journal of Fluids and Structures 1 (2), 185-196.

Dahl, J.M., Hover, F.S., Triantafyllou, M.S., 2006. Two-degree-of-freedom vortex-induced vibrations using a force assisted apparatus. Journal of Fluids and Structures 22 (6-7), 807-818.

Dahl, J.M., Hover, F.S., Triantafyllou, M.S., Oakley, O.H., 2010. Dual resonance in vortex-induced vibrations at subcritical and supercritical Reynolds numbers, Journal of Fluid Mechanics, pp. 395-424.

Facchinetti, M.L., de Langre, E., Biolley, F., 2004. Coupling of structure and wake oscillators in vortex-induced vibrations. Journal of Fluids and Structures 19 (2), 123-140.

Farshidianfar, A., Zanganeh, H., 2010. A modified wake oscillator model for vortex-induced vibration of circular cylinders for a wide range of mass-damping ratio. Journal of Fluids and Structures 26 (3), 430-441.

Gabbai, R.D., Benaroya, H., 2005. An overview of modeling and experiments of vortex-induced vibration of circular cylinders. Journal of Sound and Vibration 282 (3-5), 575-616.

Govardhan, R., Williamson, C., 2006. Defining the 'modified Griffin plot' in vortex-induced vibration: revealing the effect of Reynolds number using controlled damping. Journal of Fluid Mechanics 561, 147-180.

Govardhan, R., Williamson, C.H.K., 2000. Modes of vortex formation and frequency response of a freely vibrating cylinder. Journal of Fluid Mechanics 420, 85-130.

Govardhan, R., Williamson, C.H.K., 2002. Resonance forever: existence of a critical mass and an infinite regime of resonance in vortex-induced vibration. Journal of Fluid Mechanics 473 (1), 147-166.

Hartlen, R.T., Currie, I.G., 1970. Lift-oscillator model of vortex induced vibration. Journal of the Engineering Mechanics 96 (5), 577–591.

Hover, F.S., 1998. The lock-in phenomena for cylinders with nonlinear compliance, Internation Conference on Bluff Body Wakes and Vortex-Induced Vibrations, Washington D.C.

Jauvtis, N., Williamson, C.H.K., 2004. The effect of two degrees of freedom on vortex-induced vibration at low mass and damping. Journal of Fluid Mechanics 509, 23-62.

Jeon, D., Gharib, M., 2001. On circular cylinders undergoing two-degree-of-freedom forced motions. Journal of Fluids and Structures 15 (3–4), 533-541.

Karanth, D., Rankin, G.W., Sridhar, K., 1995. Computational study of flow past a cylinder with combined in-line and transverse oscillation. Computational Mechanics 16 (1), 1-10.

Khalak, A., Williamson, C.H.K., 1999. Motions, forces and mode transitions in vortex-induced vibrations at low mass-damping. Journal of Fluids and Structures 13 (7–8), 813-851.

Kheirkhah, S., Yarusevych, S., Narasimhan, S., 2012. Orbiting response in vortex-induced vibrations of a two-degree-of-freedom pivoted circular cylinder. Journal of Fluids and Structures 28 (0), 343-358.

Klamo, J.T., Leonard, A., Roshko, A., 2006. The effects of damping on the amplitude and frequency response of a freely vibrating cylinder in cross-flow. Journal of Fluids and Structures 22 (6–7), 845-856.

Leong, C.M., Wei, T., 2008. Two-degree-of-freedom vortex-induced vibration of a pivoted cylinder below critical mass ratio. Proceedings of the Royal Society A: Mathematical, Physical and Engineering Science 464 (2099), 2907-2927.

Moe, G., Wu, Z.J., 1990. The lift force on a cylinder vibrating in a current. Journal of Offshore Mechanics and Arctic Engineering 112 (4), 297-303.

Nayfeh, A.H., 1993. Introduction to perturbation techniques. Wiley, New York.

Noack, B.R., Ohle, F., Eckelmann, H., 1991. On cell formation in vortex streets. Journal of Fluid Mechanics 227, 293-308.

Raj, S.P., Rajasekar, S., 1997. Migration control in two coupled Duffing oscillators. Physical Review E 55 (5), 6237-6240.

Sarpkaya, T., 1995. Hydrodynamic damping, flow-induced oscillations, and biharmonic response. Journal of Offshore Mechanics and Arctic Engineering 117 (4), 232-238.

Sarpkaya, T., 2004. A critical review of the intrinsic nature of vortex-induced vibrations. Journal of Fluids and Structures 19 (4), 389-447.

Skop, R.A., Balasubramanian, S., 1997. A new twist on an old model for vortex-excited vibrations. Journal of Fluids and Structures 11 (4), 395-412.

Srinil, N., 2010. Multi-mode interactions in vortex-induced vibrations of flexible curved/straight structures with geometric nonlinearities. Journal of Fluids and Structures 26 (7–8), 1098-1122.

Srinil, N., 2011. Analysis and prediction of vortex-induced vibrations of variable-tension vertical risers in linearly sheared currents. Applied Ocean Research 33 (1), 41-53.

Srinil, N., Wiercigroch, M., O'Brien, P., 2009. Reduced-order modelling of vortex-induced vibration of catenary riser. Ocean Engineering 36 (17-18), 1404-1414.

Stappenbelt, B., 2010. Vortex-induced motion of nonlinear offshore structures: A study of catenary moored system fluid-elastic instability. Lambert Academic Publishing.

Stappenbelt, B., 2011. Vortex-induced motion of non-linear compliant low aspect ratio cylindrical systems. International Journal of Offshore and Polar Engineering 21 (4), 280-286.

Stappenbelt, B., Lalji, F., Tan, G., 2007. Low mass ratio vortex-induced motion, The 16th Australasian Fluid Mechanics Conference, Gold Coast, Australia,, pp. 1491-1497.

Vandiver, J.K., Jong, J.Y., 1987. The relationship between in-line and cross-flow vortex-induced vibration of cylinders. Journal of Fluids and Structures 1 (4), 381-399.

Wang, X.Q., So, R.M.C., Chan, K.T., 2003. A non-linear fluid force model for vortex-induced vibration of an elastic cylinder. Journal of Sound and Vibration 260 (2), 287-305.

Williamson, C.H.K., Govardhan, R., 2004. Vortex-induced vibrations. Annual Review of Fluid Mechanics 36, 413-455.

Table Captions

Table 1 Considered various ξ and m^* based on experimental input data of (a) Blevins and Coughran (2009) for a given m^* = 5.4 and (b) Stappenbelt et al. (2007) for a given ξ = 0.006, along with the tuned ε_y from associated model simulations.

Table 2 Potential effect of geometrically-nonlinear terms on 2-D VIV response prediction.

Table 3 Potential effect of empirical coefficients on 2-D VIV response prediction.

Figure Captions

Figure 1 A schematic model of a flexibly-mounted circular cylinder undergoing cross-flow/in-line VIV due to fluid lift/drag forces exerted on the oscillating cylinder.

Figure 2 Comparison of numerical and experimental (Blevins and Coughran, 2009) cross-flow amplitudes with m^*=5.4 and f^*=1: (a) ξ = 0.002 with increasing (→) and decreasing (←) V_r; (b) varied ξ; squares denote experimental results associated with numerical results (lines) by same colors; dashed lines denote response jumps.

Figure 3 Comparison of numerical and experimental (Stappenbelt et al., 2007) cross-flow amplitudes with ξ = 0.006 and f^*=1: (a) m^*=2.36 with increasing (→) and decreasing (←) V_r; (b) varied m^*; squares denote experimental results associated with numerical results (lines) by same colors; dashed lines denote response jumps.

Figure 4 Comparison of numerical (lines) and experimental (Jauvtis and Williamson, 2004) (squares) cross-flow amplitudes by using the derived ε_y functions depending on mass $\varepsilon_y(m^*)$, damping $\varepsilon_y(\xi)$ and mass-damping $\varepsilon_y(m^*\xi)$: (a) m^*=2.6, ξ = 0.0025, f^*=1; and (b) m^*=7, ξ = 0.0007, f^*=1; dashed lines denote response jumps.

Figure 5 Comparison of numerical (lines) and experimental (Stappenbelt et al., 2007) (squares) amplitudes with m^*=2.36, ξ = 0.006 and f^*=1, by considering the effect of geometrical nonlinear terms: (a) A_x/D and (b) A_y/D; dashed lines denote response jumps.

Figure 6 Effect of geometrical nonlinear terms based on experimental input data of Stappenbelt et al. (2007) with m^*=2.36, ξ = 0.006 and f^*=2: (a) A_x/D and (b) A_y/D; dashed lines denote response jumps.

Figure 7 Comparison of numerical (lines) and experimental (Stappenbelt et al., 2007) (squares) amplitudes with m^*=2.36, ξ = 0.006 and f^*=1, by considering the effect of wake-cylinder coupling terms and in-line wake coefficient: (a) A_x/D and (b) A_y/D for varied Λ_y, (c) A_x/D and (d) A_y/D for varied Λ_x, (e) A_x/D and (f) A_y/D for varied ε_x; dashed lines denote response jumps.

Figure 8 Comparison of numerical (lines) and experimental (symbols) in-line amplitudes with (a) m^*=5.4 and f^*=1 (Blevins and Coughran, 2009), (b) ξ = 0.006 and f^*=1 (Stappenbelt

et al., 2007), (c) varied $m^*\xi$ and f^*=1 (Jauvtis and Williamson, 2004): experimental results associated with numerical results by same colors; dashed lines denote response jumps.

Figure 9 Comparison of numerical (lines) and experimental (symbols) maximum attainable amplitudes (a, b) and corresponding reduced velocities (c, d) versus S_G for given m^*=2.5 and 7, f^*=1 and 2: (a) and (b) are so-called Griffin plots.

Figure 10 Comparison of numerical and experimental maximum attainable (a) cross-flow and (b) in-line amplitudes with varying m^*.

Figure 11 Three-dimensional plots of (a, b) cross-flow and (c, d) in-line amplitudes with varied m^* and V_r for given ξ=0.001: f^*=1 (a, c) and f^*=2 (b, d).

Figure 12 2-D trajectories based on experimental input data of Stappenbelt et al. (2007) with m^* = 2.36, ξ = 0.006 and f^* = 1: (a) V_r = 8, (b) V_r = 9.25, (c) V_r =9.45, with blue (red) lines denoting increasing (decreasing) V_r case; (d) V_r = 9.45 with assumed equal cross-flow/in-line wake frequencies (blue lines) and neglected quadratic nonlinear terms (dotted lines).

Figure 13 2-D trajectories based on experimental input data of Blevins and Coughran (2009) with m^* = 5.4, ξ = 0.002 and various f^*: (a) V_r = 4.5, (b) V_r = 6, (c) V_r =7; (d) V_r =7.6.

Table 1

(a)

ξ	$m^*\xi$	ε_y
0.002	0.0108	0.0055
0.02	0.1080	0.0053
0.05	0.2700	0.0067
0.1	0.5400	0.015
0.2	1.0800	0.027
0.4	2.1600	0.02

(b)

m^*	$m^*\xi$	ε_y
2.36	0.0142	0.0044
3.68	0.0221	0.0062
5.19	0.0311	0.0078
6.54	0.0392	0.0095
7.91	0.0457	0.014
8.76	0.0526	0.017
10.63	0.0638	0.027
12.96	0.0778	0.045

Table 2

Modelled Terms	Type of Nonlinearities	Potential Effect
$\alpha_x x^3, \beta_x xy^2$	Cubic (in-line equation)	Quantitative effect on cross-flow/in-line VIV response
$\alpha_y y^3, \beta_y yx^2$	Cubic (cross-flow equation)	Quantitative and qualitative effect on cross-flow/in-line VIV response
$q\dot{y}, p\dot{y}$	Quadratic (in-line/cross-flow equations)	Figure-of-eight appearance

Table 3

Coefficients	Potential Effect	
	Cross-flow VIV	In-line VIV
ε_x	Low	High
ε_y	High	High
Λ_x	Low	Low
Λ_y	High	High

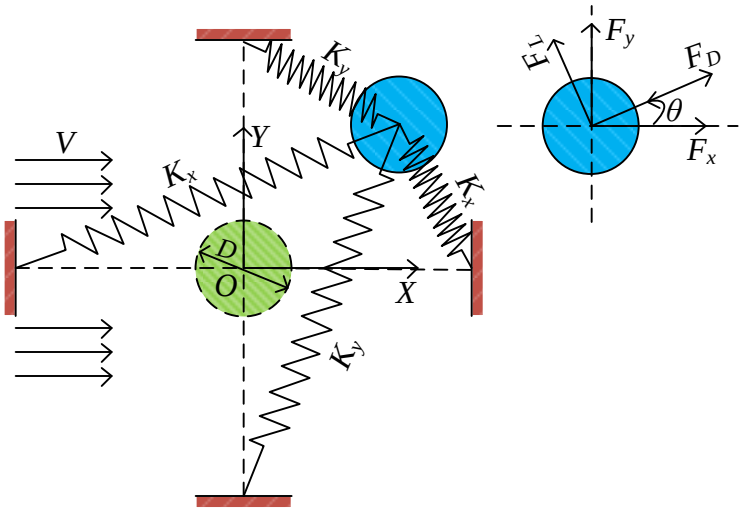

Figure 1

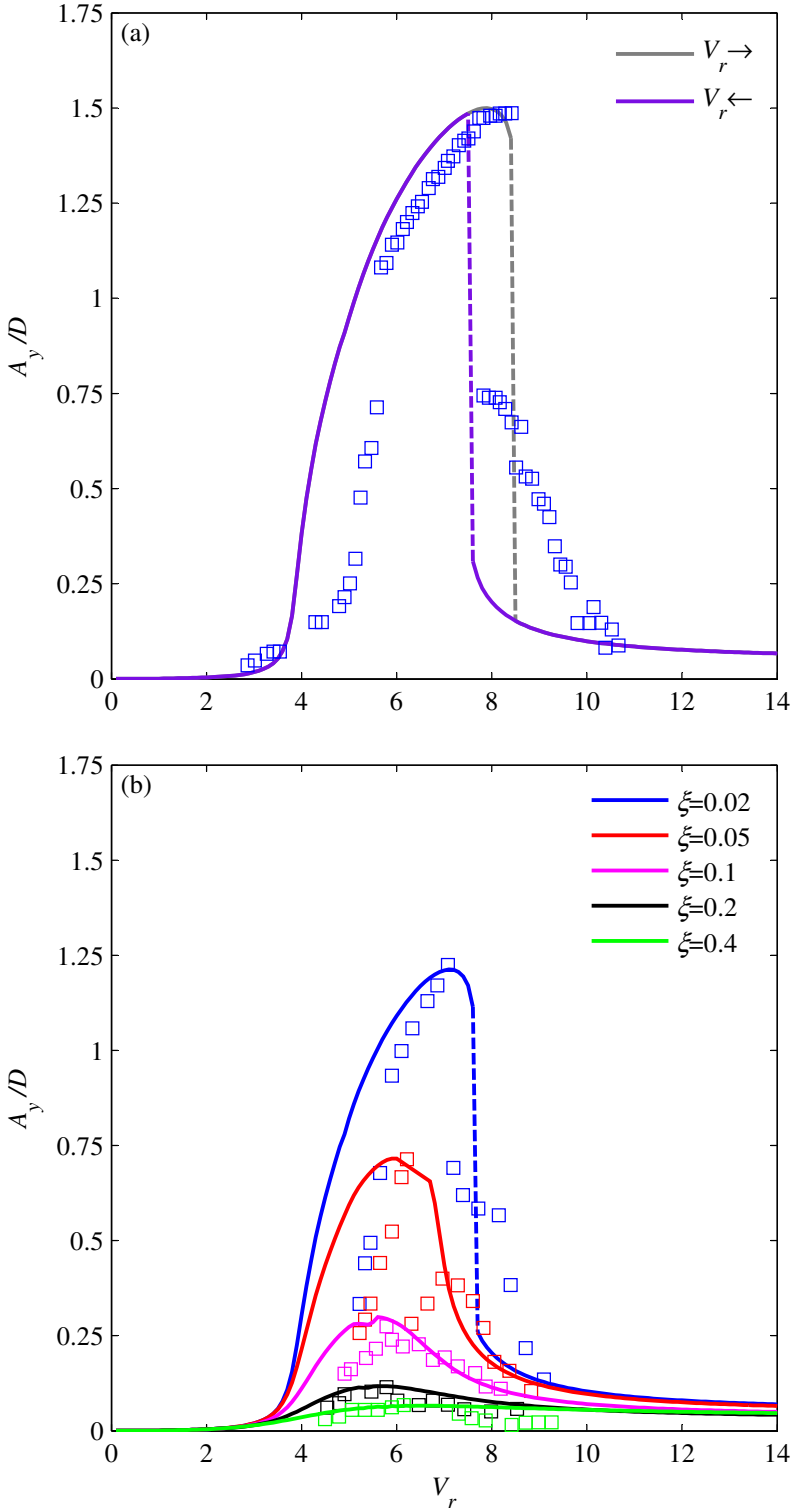
(a)
$V_r\rightarrow$
$V_r\leftarrow$
A_y/D
(b)
ξ=0.02
ξ=0.05
ξ=0.1
ξ=0.2
ξ=0.4
A_y/D
V_r

Figure 2

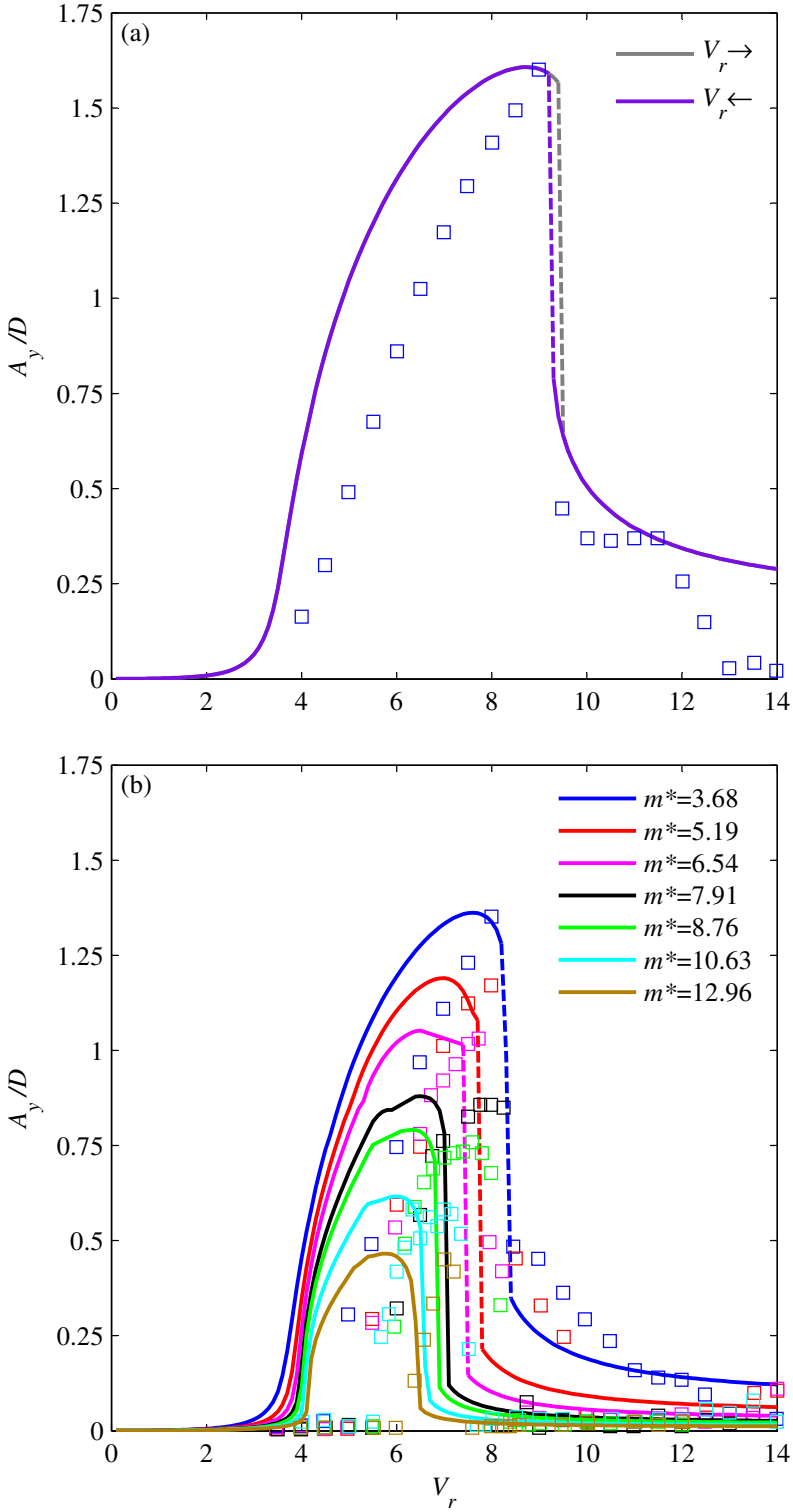
(a)
$V_r\rightarrow$
$V_r\leftarrow$
A_y/D
(b)
m^*=3.68
m^*=5.19
m^*=6.54
m^*=7.91
m^*=8.76
m^*=10.63
m^*=12.96
A_y/D
V_r

Figure 3

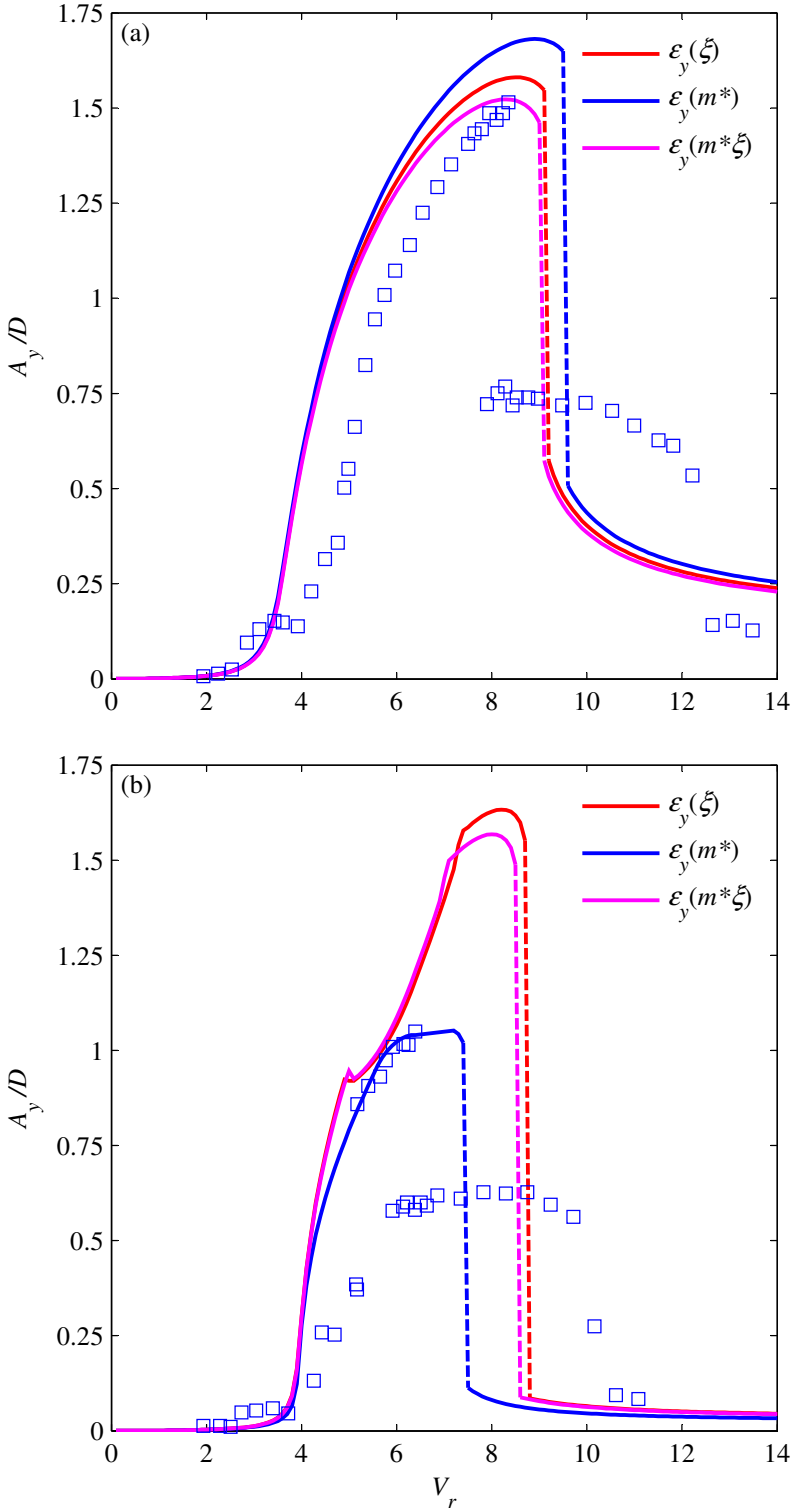
(a)
(b)
$\varepsilon_y(\xi)$
$\varepsilon_y(m^*)$
$\varepsilon_y(m^*\xi)$
A_y/D
V_r
0
0.25
0.5
0.75
1
1.25
1.5
1.75
2
4
6
8
10
12
14

Figure 4

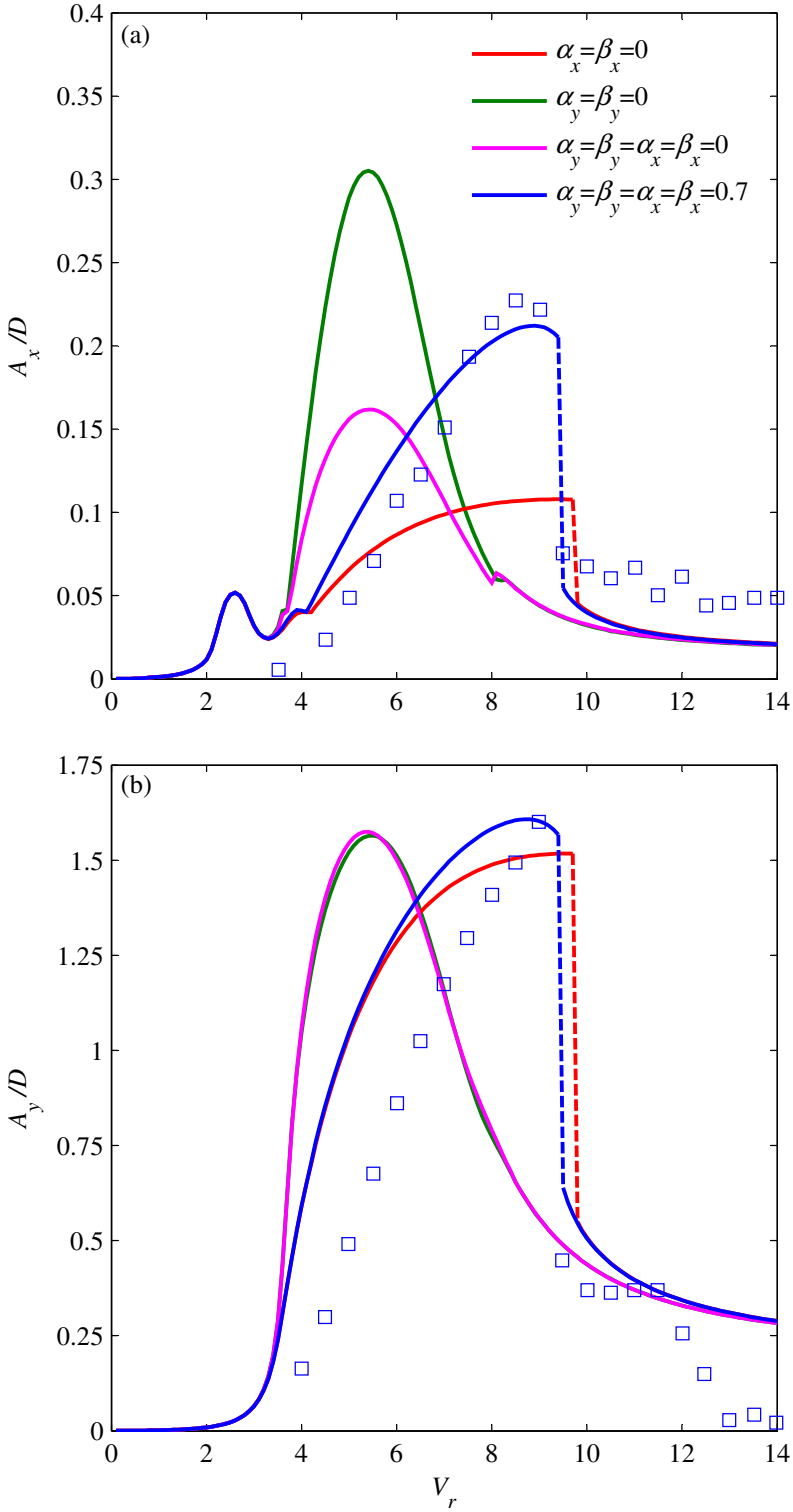
(a)
$\alpha_x=\beta_x=0$
$\alpha_y=\beta_y=0$
$\alpha_y=\beta_y=\alpha_x=\beta_x=0$
$\alpha_y=\beta_y=\alpha_x=\beta_x=0.7$
A_x/D
0.4
0.35
0.3
0.25
0.2
0.15
0.1
0.05
0
0
2
4
6
8
10
12
14
(b)
A_y/D
1.75
1.5
1.25
1
0.75
0.5
0.25
0
0
2
4
6
8
10
12
14
V_r

Figure 5

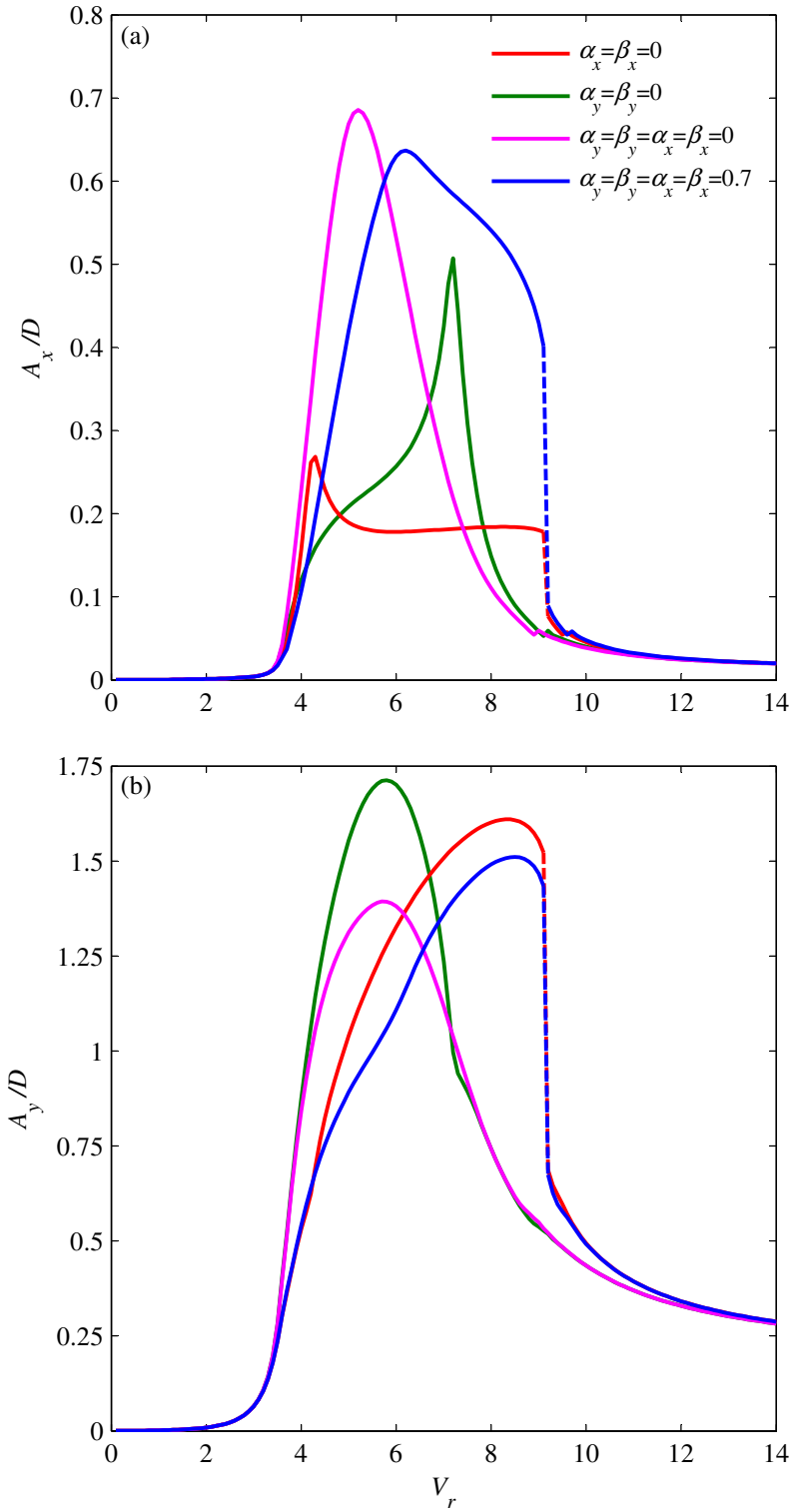
(a)
$\alpha_x=\beta_x=0$
$\alpha_y=\beta_y=0$
$\alpha_y=\beta_y=\alpha_x=\beta_x=0$
$\alpha_y=\beta_y=\alpha_x=\beta_x=0.7$
A_x/D
0.8
0.7
0.6
0.5
0.4
0.3
0.2
0.1
0
0
2
4
6
8
10
12
14
(b)
A_y/D
1.75
1.5
1.25
1
0.75
0.5
0.25
0
0
2
4
6
8
10
12
14
V_r

Figure 6

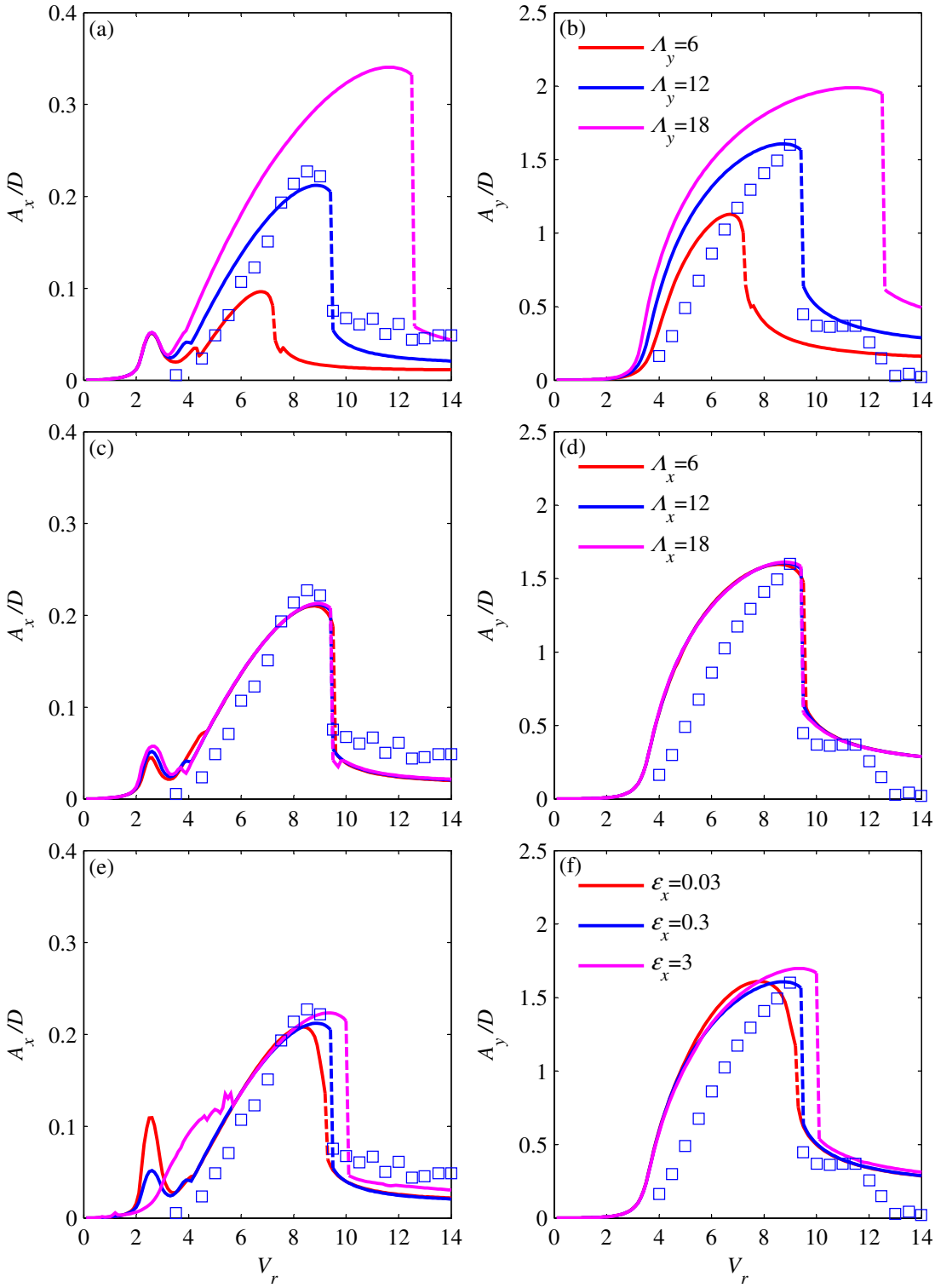
(a)
(b)
(c)
(d)
(e)
(f)
A_x/D
A_y/D
V_r
Λ_y=6
Λ_y=12
Λ_y=18
Λ_x=6
Λ_x=12
Λ_x=18
ε_x=0.03
ε_x=0.3
ε_x=3

Figure 7

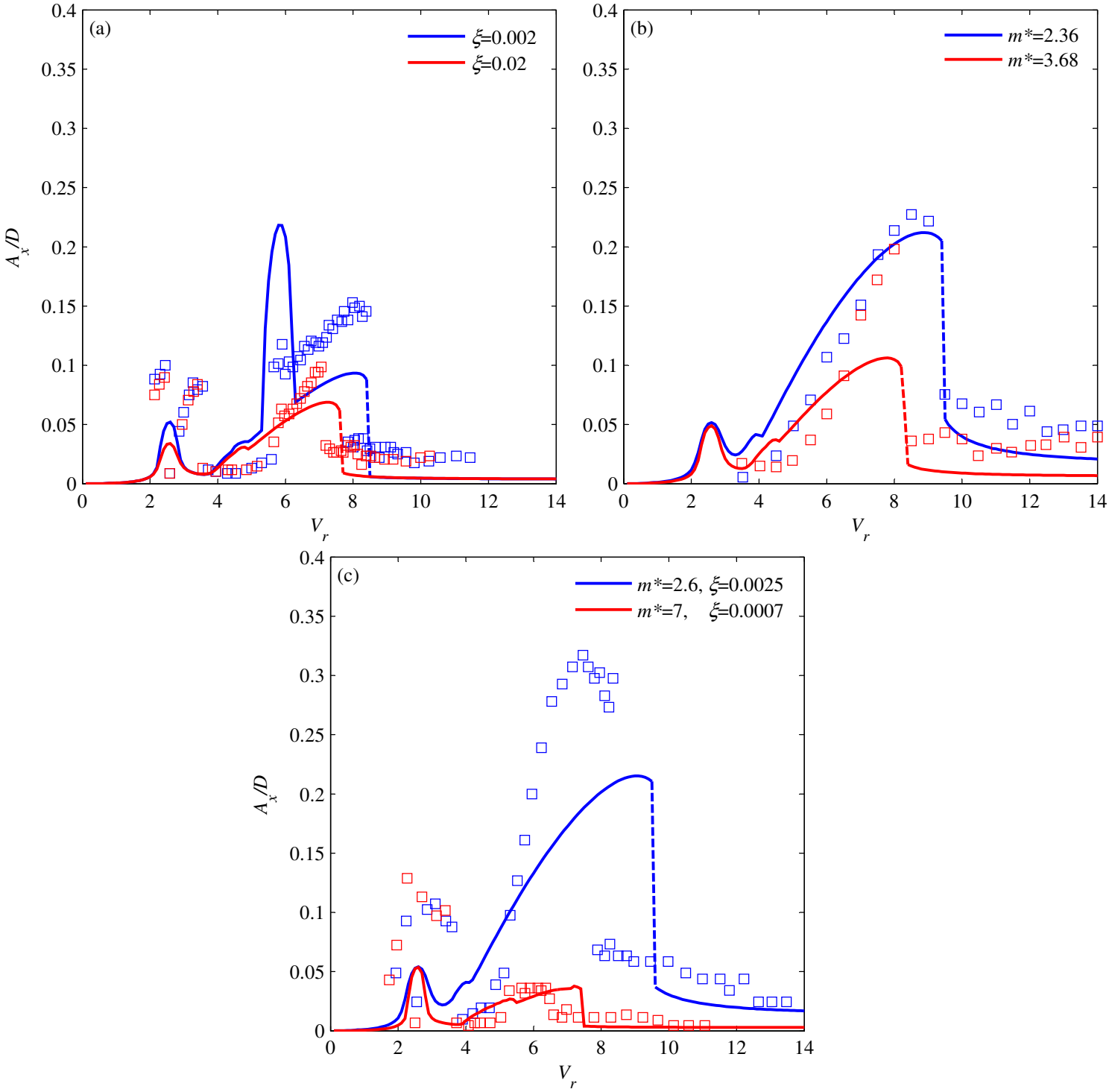

Figure 8

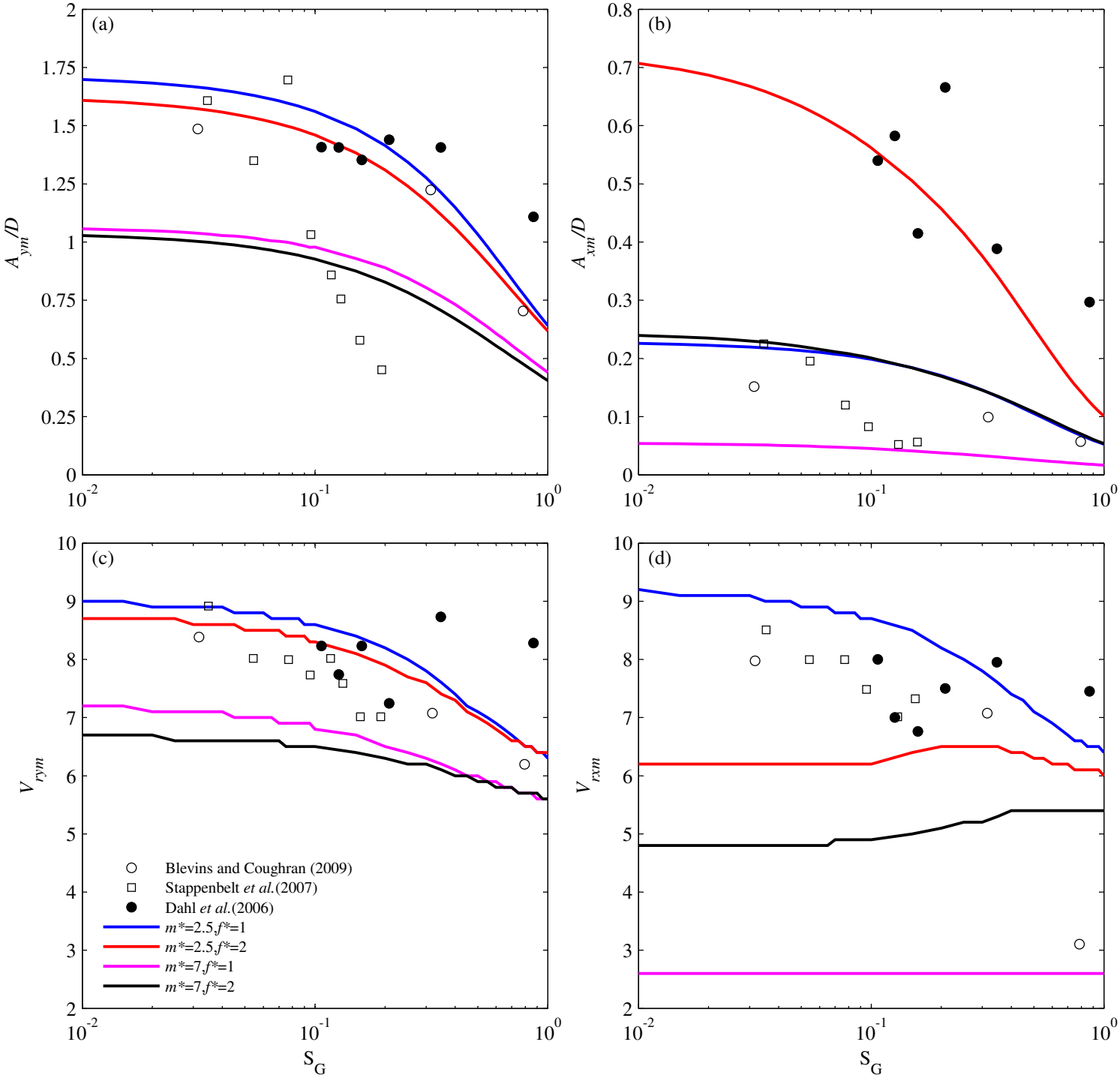
(a)
(b)
(c)
(d)
A_{ym}/D
A_{xm}/D
V_{rym}
V_{rxm}
S_G
Blevins and Coughran (2009)
Stappenbelt *et al.*(2007)
Dahl *et al.*(2006)
m^*=2.5,f^*=1
m^*=2.5,f^*=2
m^*=7,f^*=1
m^*=7,f^*=2

Figure 9

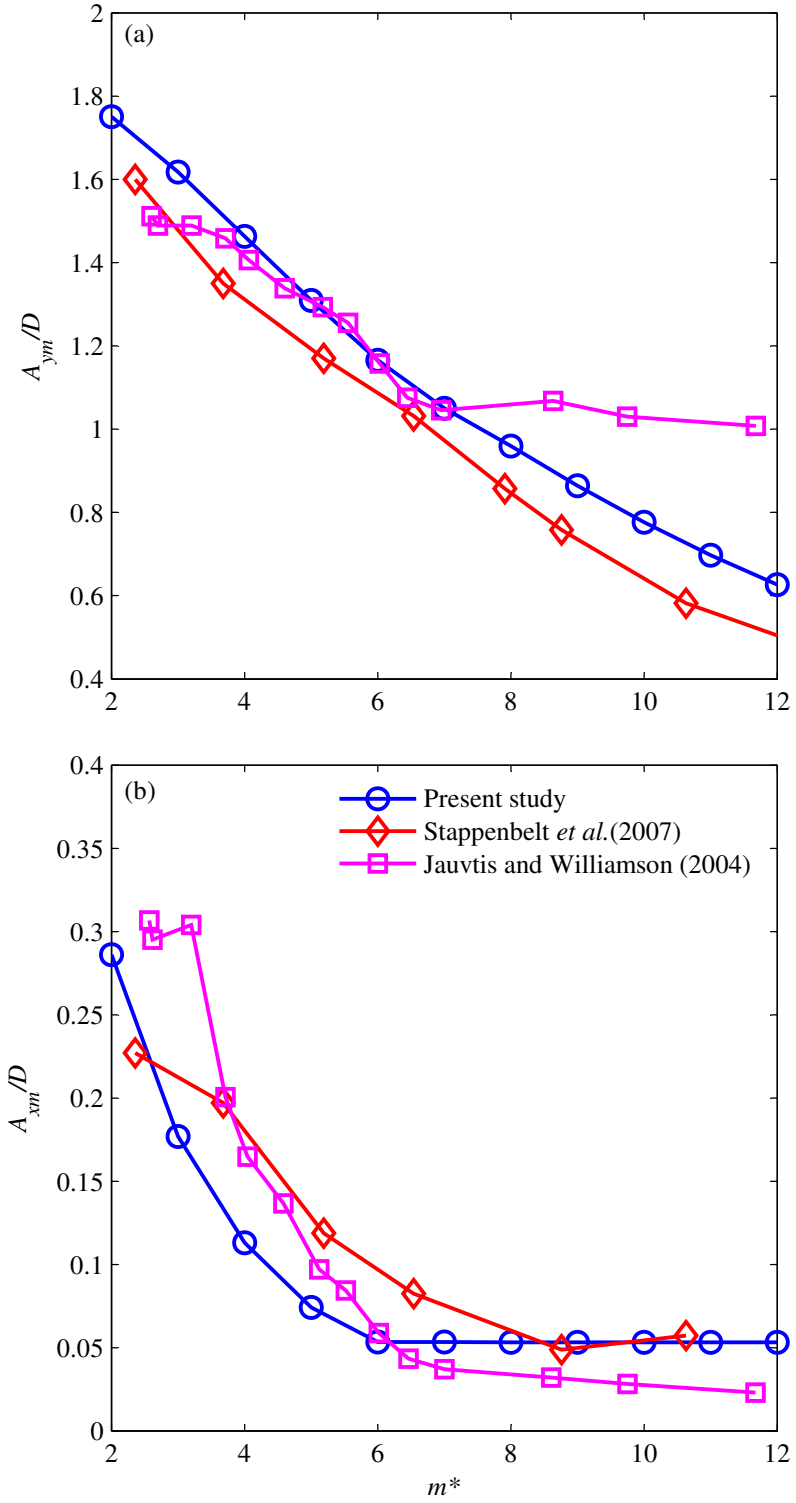
(a)
A_{ym}/D
(b)
A_{xm}/D
Present study
Stappenbelt *et al.*(2007)
Jauvtis and Williamson (2004)
m^*

Figure 10

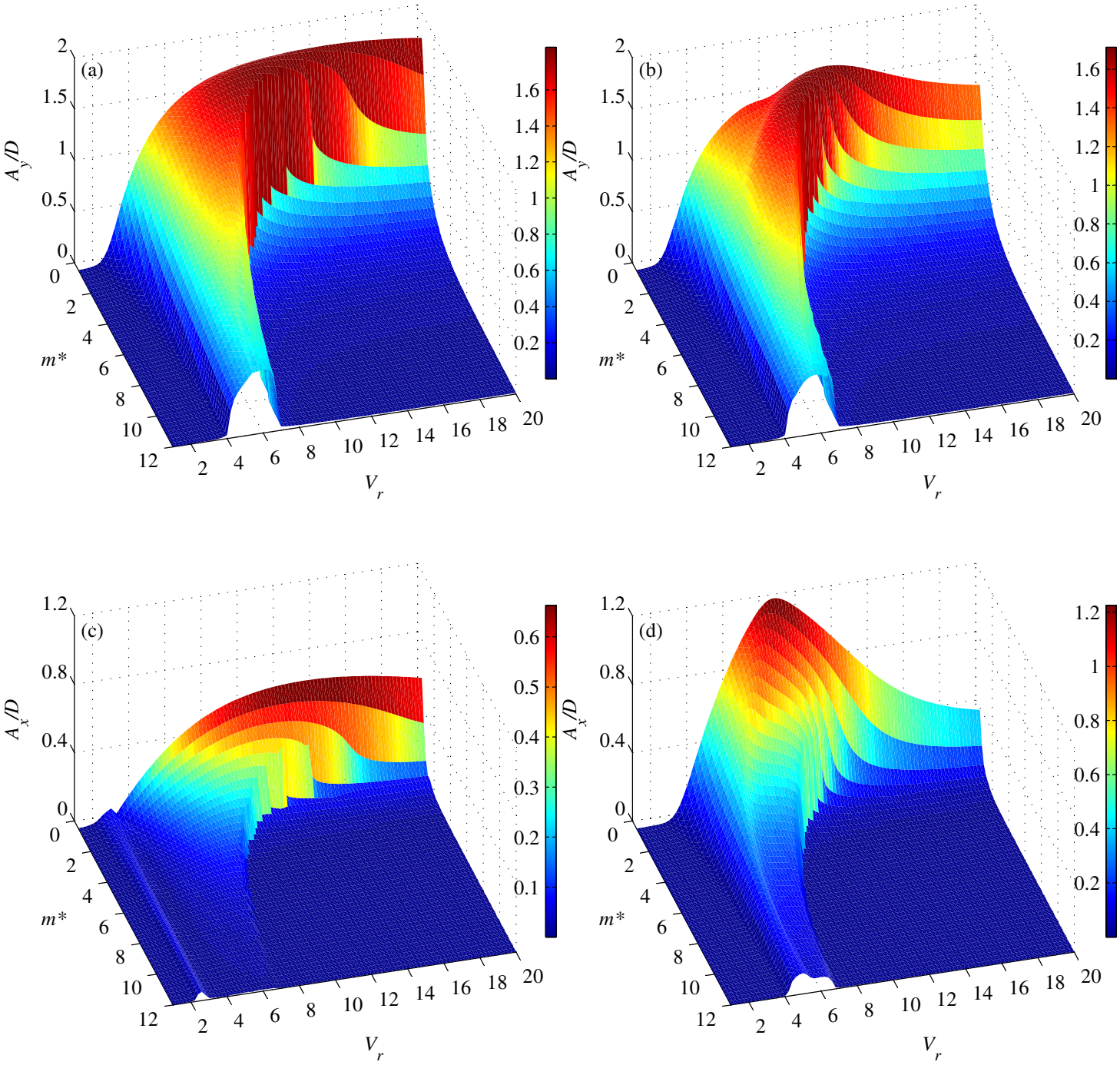

Figure 11

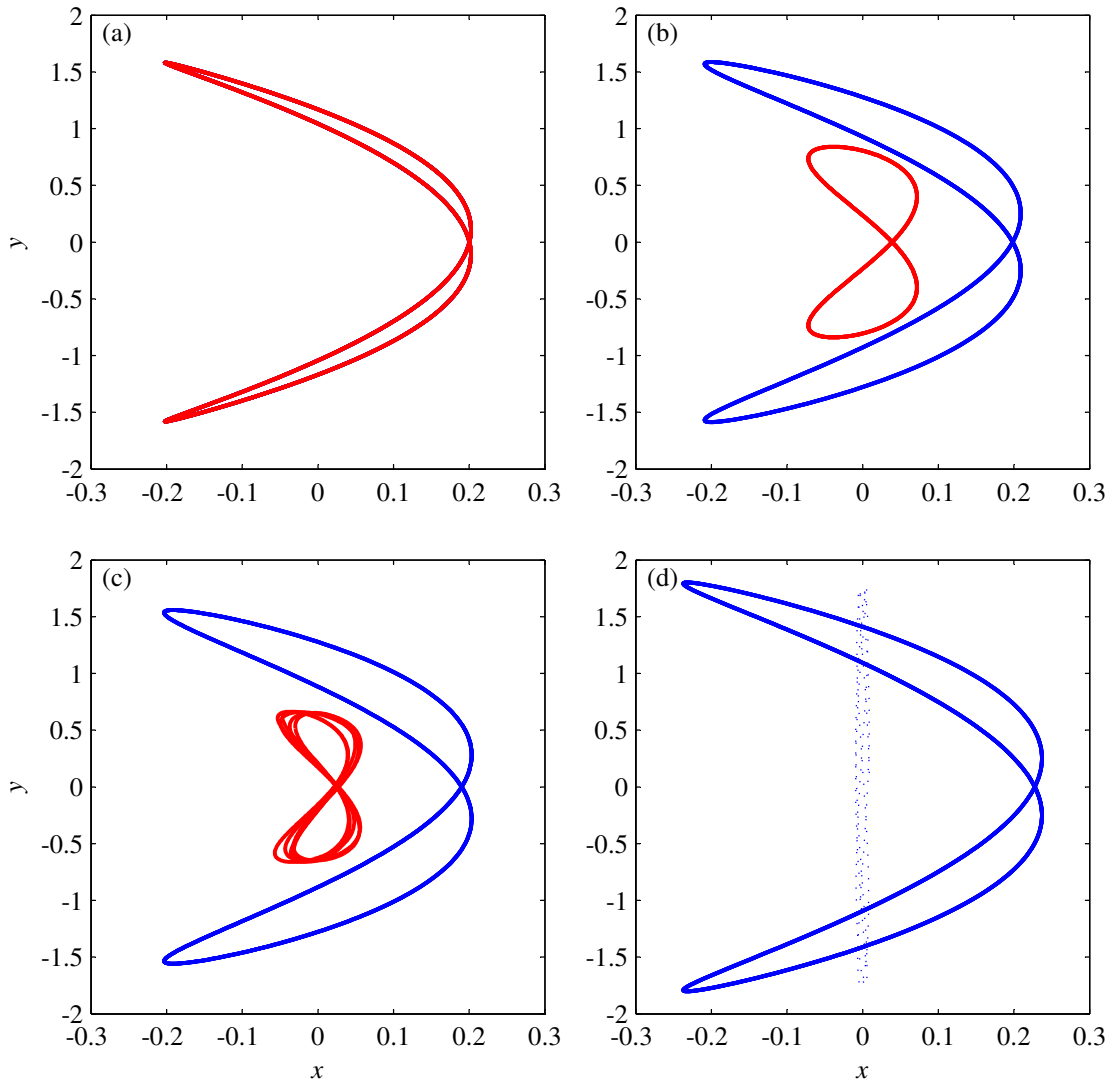

Figure 12

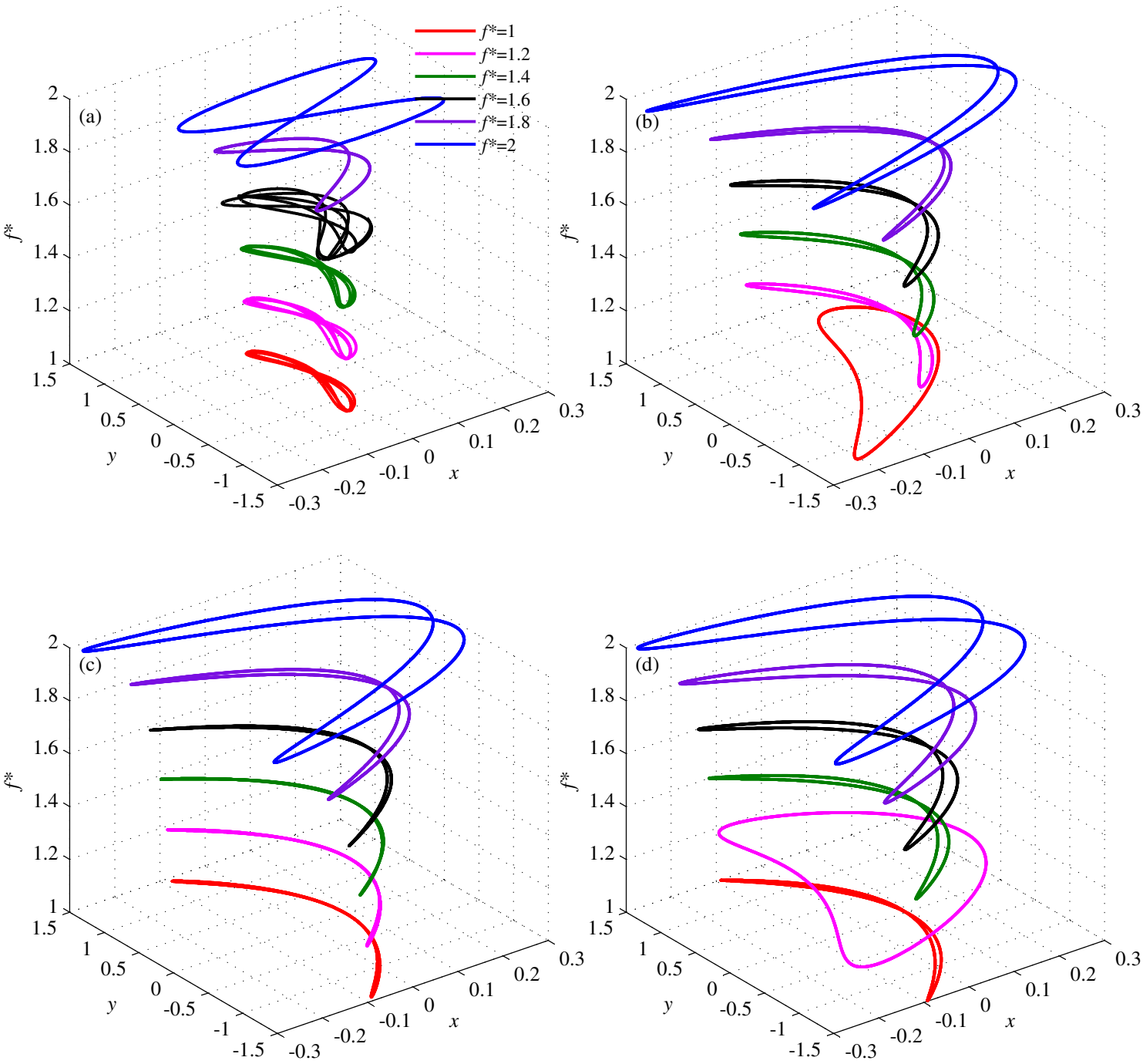

Figure 13